submitted to: www.osti.gov/elink-2413

Federal Grant Number: DE-FE0031189

Final Scientific/Technical Report

Operating Stresses and their Effects on Degradation of LSM-Based SOFC Cathodes

PD/PI and Submitting Official: Mark De Guire, Associate Professor (mrd2@case.edu, (216) 368-4221)

Department of Materials Science and Engineering

Case Western Reserve University

10900 Euclid Avenue

Office of Sponsored Projects Administration

Cleveland OH 44106-7015

submitted 29 June 2021

DUNS Number: 077758407

Project/Grant Period: 01 October 2014 – 31 March 2019

Reporting Period End Date: 31 March 2021

Report Frequency: final

Acknowledgment: This research is based upon work supported by the U. S. Department of Energy, National Energy Technology Laboratory, under the SECA Core Technology Program (award number DE-FE0031189).

Operating Stresses and their Effects on Degradation of LSM Based SOFC Cathodes

Executive Summary

The overall goals of the program were:

- To understand how selected operational parameters affect the performance of solid oxide fuel cells (SOFCs), with a focus on parameters affecting cathodes (air electrodes) comprised of lanthanum strontium manganite (LSM, $(La_{1-x}Sr_x)_{1-y}MnO_{3\pm\delta}$) and yttria-stabilized zirconia (YSZ, $(Zr_{1-z}Y_z)O_{2\pm\delta}$).
- To relate the observed relationships between operational parameters and cell performance to the microstructural changes that can be observed in the cells after operation.

This project shared these overall goals with its predecessor, DE-0023476, "Long Term Degradation of LSM Based SOFC Cathodes: Use of a Proven Accelerated Test Regimen." That project compared the effects of operating cells under "accelerated conditions" (elevated current density and temperature) versus more conventional conditions for (typically) up to 500 h, but always with humidified air as the cathode atmosphere.

The current program added reduced oxygen partial pressure p_{O_2} as an operating variable for the cathode conditions. It also included aging tests — long-term operation of the cells under open circuit voltage (i.e. zero current density) as a way to separate the effects of ambient conditions (temperature and p_{O_2}) from the effects of operation under load on how the cells' performance and microstructures change with time. Both the prior project and the current project looked at three different LSM cathode compositions that varied slightly in their degree of manganese excess, i.e. the ratio $1/(1-y)$ in $(La_{1-x}Sr_x)_{1-y}MnO_{3\pm\delta}$.

The program completed several tests under various combinations of the selected operating variables and LSM compositions. Significant findings can be summarized as follows:

- Reduced oxygen partial pressure ($p_{O_2} \leq 0.15$) is a significant operating stress on solid oxide fuel cells, greatly decreasing their operating lifetime and leading to earlier appearance of certain microstructural changes that may be relevant in degradation of cell performance.
- Cell-to-cell variations can lead to differences in long-term performance that are as large as or larger than the effects of cathode composition, over the range of LSM compositions studied here.
- Trends in the area specific resistance (ASR) of these SOFCs with time could be traced using periodic electrochemical impedance spectroscopy (EIS) and linear sweep voltammetry (LSV) as well as direct observations from cell output voltage versus time.
- Distribution of relaxation times (DRT) analysis of the EIS results showed that electrode loss mechanisms, with characteristic frequencies in the ranges of 10^{-1} to 10^{3} Hz, can be associated with reaction and transport processes at the anode and cathode of SOFCs.

Project Participants

Project Director and Principal Investigator: Mark R. De Guire, Ph.D. Associate Professor, Department of Materials Science and Engineering, Case Western Reserve University

Other senior investigator: Arthur H. Heuer, Ph.D., Distinguished University Professor and Kyocera Professor of Materials, Department of Materials Science and Engineering, CWRU (until 2019)

Graduate (M.S.) students (CWRU): Chenxin Deng, Thomas Dietrick

Undergraduate researchers (CWRU): Madeleine McAllister, Jen Bradley, Sipei Li, Zachary Fong

Summary of Project Activities

Background and hypotheses

This work (and the prior project[1]) focused on the air electrode (cathode), as loss of performance in SOFC cathodes is a main contributor to degradation of cell performance during extended operation [1–14]. Our prior study described the use of higher-than-normal operating temperature (1000 °C) and current density (780 mA cm^{-2}) in air as "accelerated testing." In such approaches, the unavoidable question [15,16] is whether the accelerated conditions accurately replicate in shorter times the actual long-term operation (and the accompanying degradation) of cells operated under normal conditions for longer times. Recognizing this uncertainty, the proposed work adopts the term "aggressive" (rather than "accelerated") conditions, and continues to contrast them with "conventional" conditions in their effects on cell performance and the accompanying microstructural changes. The values of temperature, current density, and partial pressure of oxygen p_{O_2} used in the previous and the current projects, as well as the conditions for aging testing, are given below.

Operational parameters studied in prior work, and proposed for the new project. Green shading denotes a conventional condition; yellow shading denotes an aggressive condition.

	temperature [°C]	current density [mA cm^{-2}]	cathode p_{O_2}
prior work	900	380	0.2
	1000	760	
current work	900	380	0.1
		OCV (aging)	
	1000	760	
		OCV (aging)	

Regarding p_{O_2}, other groups have explored the effect of higher values (i.e. 100% oxygen) or very low values. Therefore this work used values of p_{O_2} between these extremes. Whereas $p_{O_2} \cong 0$ and $p_{O_2} = 1$ provide insights into the role of oxygen on cell performance, the conditions studied here are more directly relevant to operation of cells, stacks, and systems, even if a direct equivalence to long-term conventional operation might not be ascertainable.

[1] "Long Term Degradation of LSM Based SOFC Cathodes: Use of a Proven Accelerated Test Regimen," DE-FE0023476, October 2014 – March 2019.

Operation at low p_{O_2} had been explored in an earlier collaboration between LG Fuel Cell Systems (LGFCS) and CWRU [17]. Lab-scale cells with cathodes of $(La_{0.85}Sr_{0.15})_{0.90}MnO_{3\pm\delta}$ (LSM 85-90) and YSZ were tested at 800 °C in an atmosphere of 1.2% steam, 8.5–11.3% O_2 under an elevated pressure of 6.4 bars. Figure 1a–d shows the cathodes of the untested cell (Fig. 1a) and after 2,000, 8,000, and 16,000 h of testing (Fig. 1b–d) [18], obtained with transmission electron microscopy (TEM) and energy-dispersive x-ray spectroscopy (EDXS). The untested cathode showed small manganese oxide (MnO_x) particles, 0.2–0.4 µm in size, uniformly distributed across the cathode. In the course of extended testing under the low-p_{O_2} cathode atmosphere, the number and concentration of MnO_x particles increased, and porosity decreased, particularly near the cathode-electrolyte interface (left edge of each image). Beyond a distance of ~2 µm from the electrolyte, MnO_x particles were scarcer than in the untested cathode.

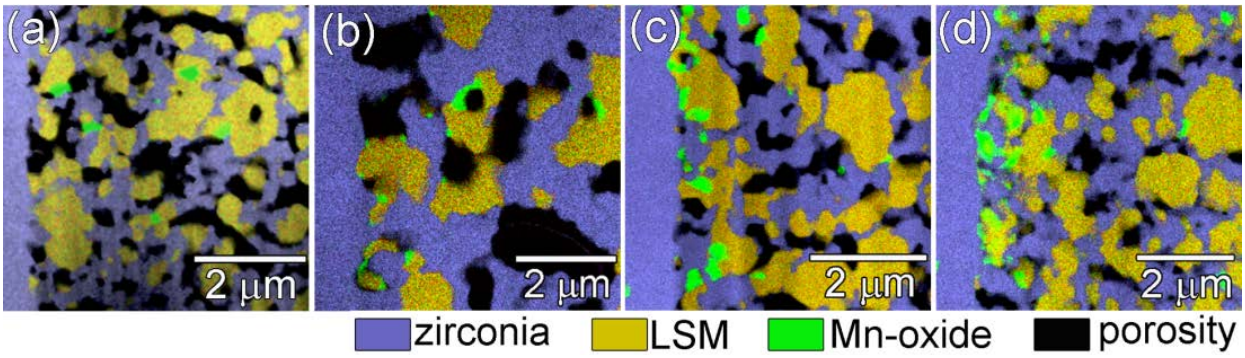

Figure 1. EDXS elemental maps acquired across the LSM 85-90 cathode-electrolyte interface for (a) an as-fired cell, (b) the 800-°C, 2-kh cell (c) the 800-°C, 8-kh cell, and (d) the 800-°C, 16-kh cell. (The electrolyte is at the left edge in each image.) YSZ is blue, LSM yellow, MnO_x green, and pores black.

LGFCS used AC electrochemical impedance spectroscopy (EIS) to show that such cathode microstructural change during testing coincides with the cell's degradation during use [17]. Such microstructural change during operation may cause degradation of cathode performance due to loss of triple phase boundaries (TPB) near the electrolyte interface (a critical region for the necessary catalytic reactions) and increased resistance for gas diffusion. This could constitute a major factor of the increasing ASR that is a principal cause of long-term degradation of LSM-based SOFCs. Overall, severe cathode microstructural change only occurred after long-term testing under the range of normal system operating conditions.

The prior project[1] at CWRU found that the distribution of MnO_x in an LSM 85-90 cathode was essentially unchanged after testing the cell in air for 500 h at 900 °C and conventional current density (0.38 A cm^{-2}) (Fig. 2, middle).[2] In contrast, when an identical cell was tested in air under aggressive temperature (1,000 °C) and current density (0.76 A cm^{-2}) for 493 h, similar microstructural changes (Fig. 2, bottom) as those seen in low-p_{O_2} operation up to 16 kh (Fig. 1) were observed. In the cathode current collector (CCC) after 493 h of aggressive testing in air, the MnO_x particles were more pronounced and were significantly coarsened compared to the as-received and

[2] A (La,Sr)-rich region (red box, middle image, Figure 2) was probably a result from an inhomogeneity in the starting cathode powder, as such features are extremely rare in over nine years of studying the microstructures of LSM cathodes at CWRU.

conventionally tested cathodes.

Besides aggressive and conventional conditions, the other main independent variable in the prior and present studies was the extent to which the ratio Mn/(La+Sr) exceeded the stoichiometric perovskite ratio of 1 in $(La_{1-x}Sr_x)_yMnO_{3\pm\delta}$, with Mn excess defined as $1/y - 1$.

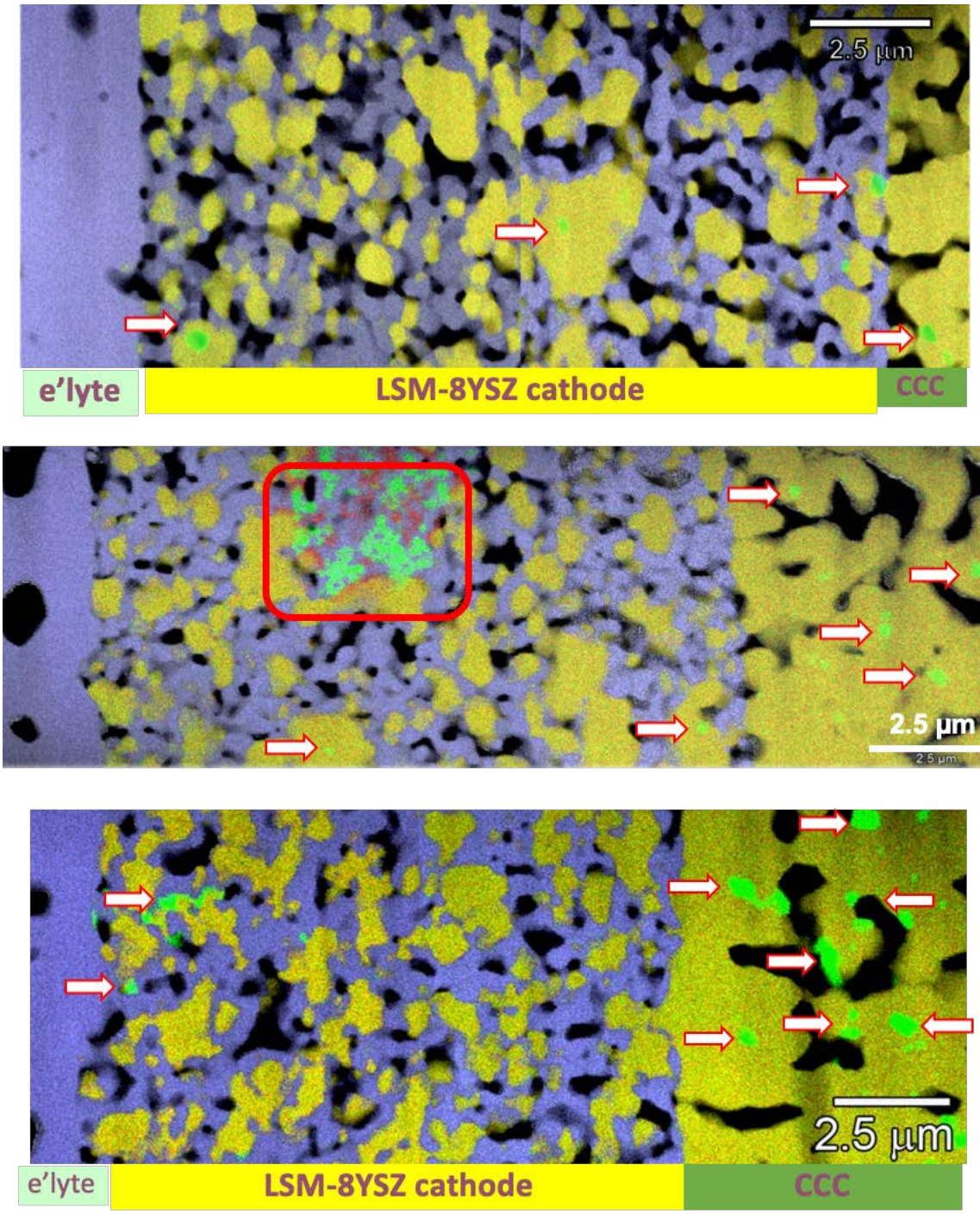

Figure 2. TEM cross-sections (with EDXS elemental maps) of cycle-1 cathodes (LSM 85–90, 11% Mn excess) as received (top), and after 500 h of conventional (middle) testing, and 493 h of accelerated testing (bottom). 8YSZ: blue; LSM: yellow; pores: black; MnO_x: green.

The objectives of this project were to:

1) Add reduced p_{O_2} to the matrix of aggressive and conventional testing conditions;
2) Conduct electrochemical aging, durability, diagnostic, and current load cycling tests on one or more cathode formulations;
3) Conduct detailed microstructural characterization, using electron microscopy and energy-dispersive x-ray spectroscopy (EDXS), on tested cells typically after 500 h or more of testing, or until cell failure, as determined by either a) output voltage of < 0.8 V at the selected current density, or b) OCV < 1.00 V;
4) Relate the performance histories of the cells and their operating conditions to the results of the microstructural studies.

Approaches used

SOFC button cells. All cells in this work were $Y_{0.08}Zr_{0.92}O_{1.96}$ (8YSZ) electrolyte-supported "button" cells and were fabricated at LGFCS. The electrolyte was 3.18 cm in diameter and 100 μm thick.[3] The anodes (nominally identical for all cells) were screen-printed porous composites of NiO and 8YSZ (60:40 wt%), 0.95 cm in diameter. (NiO was reduced to Ni under flowing H_2/N_2 during the initial heat-up of the cell before operation.) A NiO–based current collector layer was screen-printed and co-fired on each anode.

The cathodes were porous 8YSZ–LSM composites (50:50 wt%), 0.95 cm in diameter, screen-printed on the fired electrolytes, differing only in composition of the LSM phase:

- $(La_{0.85}\,Sr_{0.15})_{0.90}\,MnO_{3\pm\delta}$ (LSM 85-90) — 11% Mn excess
- $(La_{0.80}\,Sr_{0.20})_{0.95}\,MnO_{3\pm\delta}$ (LSM 80-95) — 5% Mn excess
- $(La_{0.80}\,Sr_{0.20})_{0.98}\,MnO_{3\pm\delta}$ (LSM 80-98) — 2% Mn excess

(Cells with a fourth cathode composition, proprietary to LGFCS and denoted D, were also tested.) A 100% LSM current collector layer (same composition as the LSM in the cathode) was screen-printed and co-fired on each cathode. The area of all anodes and cathodes was 0.708 cm^2.

Platinum meshes were cut to the diameter of each electrode. A platinum wire was spot-welded to each mesh. A mesh (with attached wire) was adhered to each electrode using nickel-based ink for the anode and LSM-based ink for the cathode and then fired to attach the meshes to the cell. The cell was then sealed to an 8YSZ ceramic tube using a glass paste, fired in air.

Fixture for testing in controlled cathode atmosphere. Figure 3 shows the test fixture that was designed and fabricated for this project, with button cell and platinum wire electrodes. O-rings for gripping the ceramic tubes were silicone rubber (to withstand elevated temperatures). All ceramic tubes were from McDanel Advanced Ceramic Technology, LLC.

The metal parts of the fixture were of titanium (grade 2), chosen for its high strength and oxidation resistance at the elevated temperatures encountered 3" below the furnace of our test stands. It is also significantly lighter than stainless steel, reducing the load on our support framework and making the fixture easier to insert into and remove from the furnace. Figure 4 shows the engineering drawings of these parts.

[3] For the LSM 85-90 cells tested and characterized in the prior project, the thickness of the electrolyte was 200 μm.

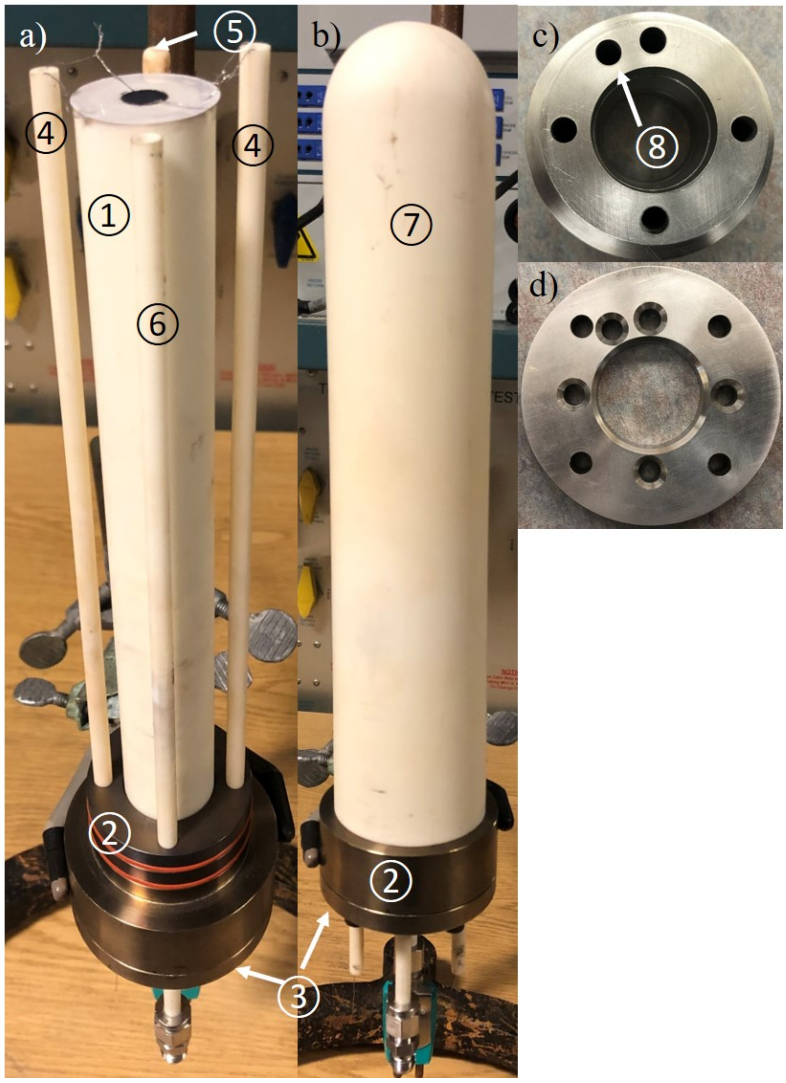

Figure 3. Button cell in the test fixture: a). Set up for testing in air. b). For testing in controlled atmosphere, an alumina tube with one closed end was placed over the set-up shown in a). c) Top view, upper part of the fixture. d) Top view, bottom part of the fixture. ① YSZ tube with cell sealed on top; ② Upper part of the test fixture; ③ Bottom part of the test fixture; ④ Double bores tube for electrode leads; ⑤ Type R thermocouple; ⑥ Cathode gas inlet tube; ⑦ Closed-end tube; ⑧ Cathode gas exhaust hole.

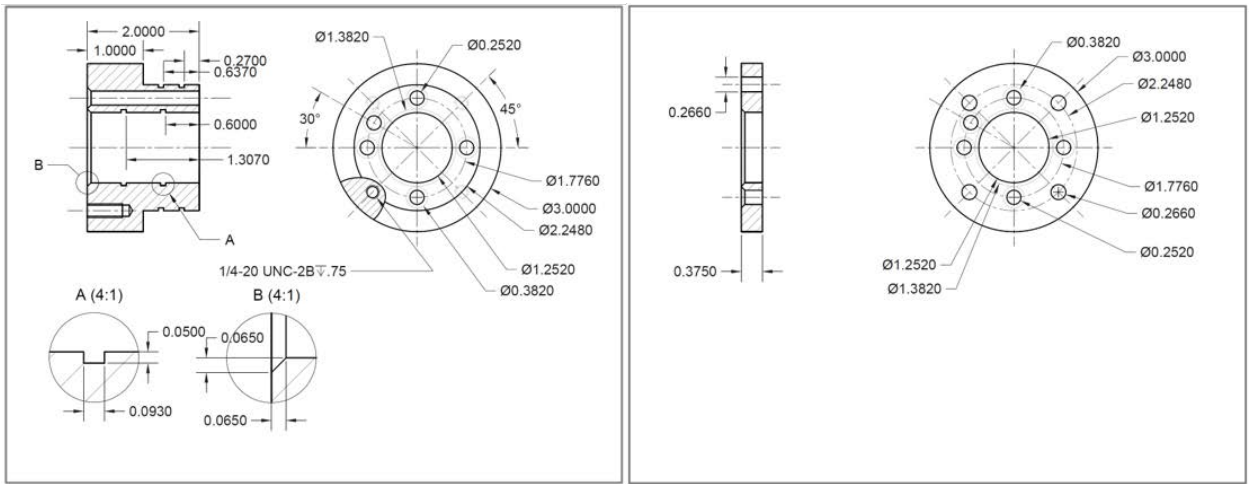

Figure 4. Engineering drawings of the titanium test fixture

During cell testing, hydrogen (50 sccm, humidified to 3% by flowing through a water bubbler held at 25 °C) was used on the anode side. For testing under controlled cathode atmosphere, the cathode gas was passed through a separate water bubbler held at 25 °C; otherwise, the cathode was exposed to ambient air. Figure 5 schematically shows the gas flow configuration for all tests (left) and the position of thermocouples during tests under controlled cathode atmosphere (right). Anode and cathode gas flows were controlled using Omega FMA5408A-ST mass flow controllers (MFC) (0–100 sccm).

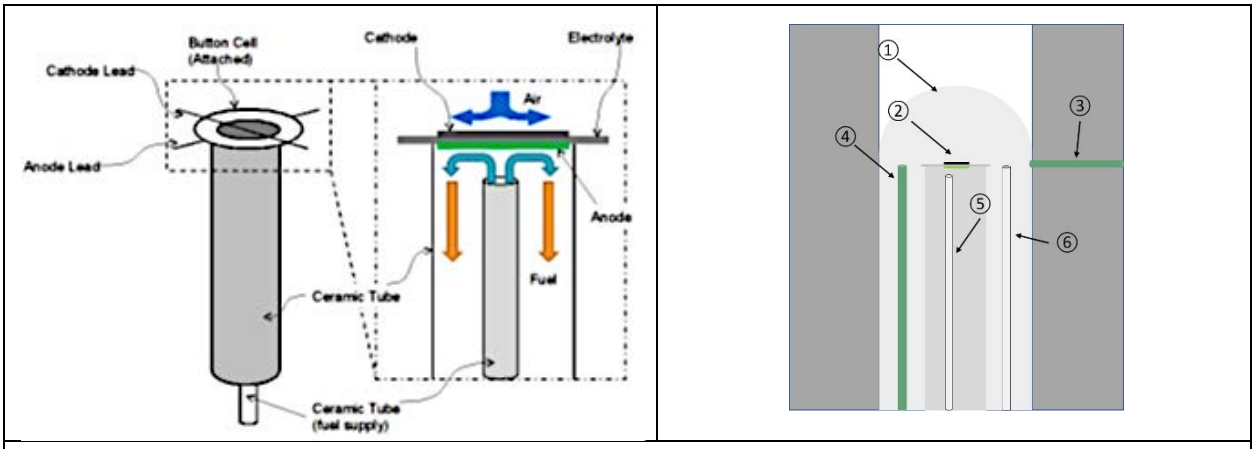

Figure 5. Left: schematic illustration of the cell configuration during testing. Right: Positioning of two thermocouples. ① Closed-end tube; ② Button cell; ③ Furnace thermocouple; ④ Cell thermocouple; ⑤ Anode gas inlet tube; ⑥ Cathode gas inlet tube.

High-temperature electrochemical measurements. Two identical test stands were available for use in this project, each with an Applied Test Systems, Inc. 3110 series vertical cylindrical furnace, controlled by an Omega CN16PT-440 digital controller through Platinum Configurator software. Tests were monitored using a Dell Optiplex 3020 workstation and monitor, equipped with two data acquisition boards (NI USB-6009,14-bit, 48kS/s, National Instruments) (NI-DAQ) running Windows 10 Enterprise, LabView (NI LabView 2018, National Instruments), and NOVA electrochemical analyzer software (versions 1.11.2 and 2.1.4, Metrohm-Autolab). An Autolab

PGSTAT302 (Metrohm-Autolab) electrochemical workstation with an additional FRA2 module (10 μHz to 1 MHz) served as the current source and provided the cell voltage readings. The cell real-time voltage, current, and flow rates of gases were collected by NI-DAQ boards, and the flow rates of gases were controlled by a LabView program. Figure 6 shows the wiring diagram of the test stand (left) and a diagram of the four-electrode configuration of the cell. Actual cell current was measured by the voltage drops across a 0.100-Ω shunt resistor that was spliced into the working electrode in series with the cell.

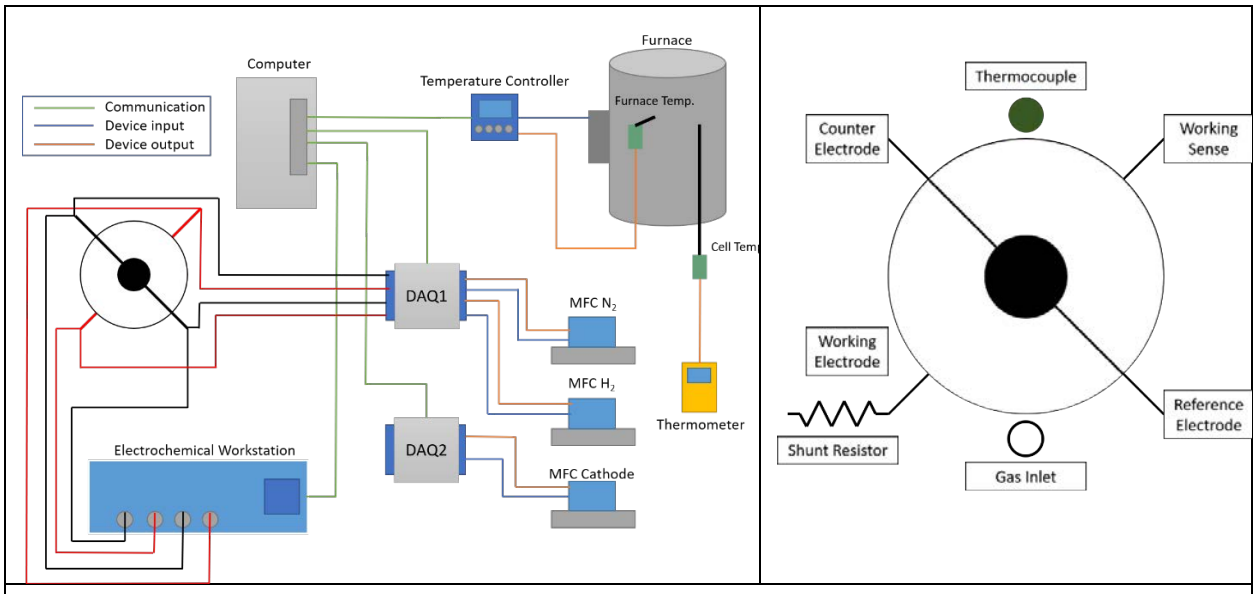

Figure 6. Left: Electric circuit system of the test stand. "MFC" denotesq a mass flow controller. "DAQ" denotes a data acquisition board. Right: Diagram of the four-electrode configuration, with 0.100-Ω shunt resistor for measuring actual cell current.

For high-temperature electrochemical measurements, the cell, mounted in the test fixture and inserted into the furnace, was heated to 1,000 °C at a rate of 3 °C min^{-1} in air on both the cathode and anode side. The anode air was gradually flushed with nitrogen (0–50 sccm in increments of 5 sccm) and held for 10 min.

To reduce the NiO in the as-received anode to Ni, the nitrogen anode feed was gradually replaced by hydrogen in increments of 5 sccm, keeping the total flow rate constant at 50 sccm. The 50 sccm hydrogen flow was held for an hour, after which the open circuit voltage (OCV) was recorded. If the OCV was above 1.00 V, the NiO was assumed to be fully reduced to Ni, and testing proceeded to the parametric test.

In parametric testing, EIS measurements (details below) were made at 1,000, 900, 850, and 800 °C. A fifth measurement was performed at 800 °C with 5 sccm hydrogen and 45 sccm nitrogen (denoted "10% H_2" in the results below). Before each of these EIS measurements, the system equilibrated at the intended temperature and atmosphere for one hour.

The galvanostatic EIS measurements were performed with the Autolab PGSTAT302 electrochemical workstation (Fig. 6) with a single sine, frequency response analyzer (FRA module) scan from 100 kHz to 0.01 Hz, changing the frequency in 10 equal increments per decade. The amplitude of current scan is 0.05 A in absolute value, and the maximum integration time was 0.125 s. These settings generated 71 different frequencies for every test.

For LSV measurements, a steadily increasing DC current was applied to the cell, and the corresponding voltage outputs of the cell were recorded. The current was increased from 0 to 0.6 A (in increments of 0.025 A) in aggressive testing, or to 0.28 A (in increments of 0.01 A) in conventional testing. The scan rate was 0.01 A/s. In total, 34 current sets were generated based on these settings (39 sets in conventional tests). The power density was calculated based on current and voltage as

$$Power\ density\ [\mathrm{mW/cm^2}] = V \times J \quad (1)$$

where V is the output voltage of the cell at current density J [mA/cm^2], i.e. the current between the working electrode and the counter electrode,[4] divided by the electrode area.

All durability tests were conducted at constant temperature T and current density J. Cell voltage $V(t)$ and current were measured every 60 s or less for the duration of the test. Every 24 h at noon, the current load was zeroed. When the OCV reading stabilized, an EIS measurement was taken, followed by linear sweep voltammetry (LSV) to obtain the cell's current–voltage (I–V) characteristic, both carried out through NOVA. Open circuit voltage $V_{OC}(t)$ (OCV) of the cell (cell output voltage under normal anode and cathode feed streams at zero current density) was recorded during every LSV measurement.

If a test reached the intended duration (500 h or longer), the current load was turned off. A final suite of parametric tests like the one done at $t = 0$ was conducted, and then the cell was cooled at open-circuit voltage to room temperature at a ramp rate of 3°C/min under a continuous flow of 50 sccm humidified H_2. If the open-circuit voltage of a cell dropped below 1.00 V at any point during durability testing, the test was terminated without final parametric tests. Additional details of the cell testing are given in [19,20].

Interpretation of EIS measurements: Equivalent circuit analysis. The testing protocol followed in this work generated many EIS spectra from each cell: from parametric tests, and from the daily EIS measurements taken during the extended test. The AC behavior of the cells, and their associated electrochemical reactions, can be modeled as an "equivalent" electric circuit that would produce an EIS spectrum matching the one obtained experimentally. Figure 7 shows a simple example that is commonly used in the literature for SOFCs.

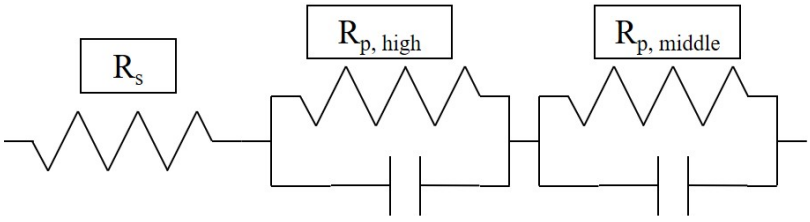

Figure 7. Simple equivalent circuit model for SOFCs.

R_S represents the series ohmic resistance of the cell, mainly attributed to oxygen ion transport in YSZ in the electrolyte and the electrodes (with smaller contributions for the DC electronic conductivity of the electrodes). $R_{P,\,middle}$ and $R_{P,\,high}$ are resistances often attributed to loss mechanisms of the anode (higher frequency) and cathode (middle frequency).

[4] This value of current is slightly different from the current generated from the electrochemical workstation.

For the results of the equivalent circuit fit to be reliable, especially for an unknown electrochemical system, the test data need to be validated before further processing. The Kramers–Kronig (K-K) relation is often used to determine the quality of an impedance measurement. In our study, the K-K test was performed using a built-in command of the NOVA software on all parametric test results.

An alternative validation is to consider the sum of the squares of the relative residuals between the measured value and the modeled value, χ^2. The scale of χ^2 depends on the value and the number of datasets. Normally, an excellent fit has a value of χ^2 less than 10^{-6}, reasonable results lie between 10^{-5} and 10^{-6}, marginal between 10^{-4} and 10^{-5}, and inadequate for higher values. In addition, the residuals should be small and randomly distributed around zero [21]. Values of χ^2 in this work were typically between 10^{-4} and 10^{-7}. This gives confidence that the simple circuit model (Figure 7) used here can be validly applied. The K–K test was also applied periodically on EIS data collected during durability testing to check that the fitting of an equivalent circuit remained valid.

Fits of EIS spectra to the equivalent circuit of Figure 7 were obtained from plots of the imaginary part of the impedance, $-Z''$, versus the real part of the impedance, Z', at each frequency (a.k.a. Nyquist plots) by using the Electrochemical Circle Fit tool in NOVA software. The value, in Ω (or, when multiplied by the area of the electrodes, in Ω cm^2) consists of a series resistance and usually two parallel resistances. In this study, the semicircle that occurred above 100 Hz was assigned to the high frequency arc ($R_{p,\,h}$), and between 100 Hz and 1 Hz is called the middle frequency range, where $R_{p,\,m}$ lies (Fig. 8). Any arc that occurred below 1 Hz was omitted from the analysis, as this part of the spectrum is due primarily to impedances unrelated to the cell itself.

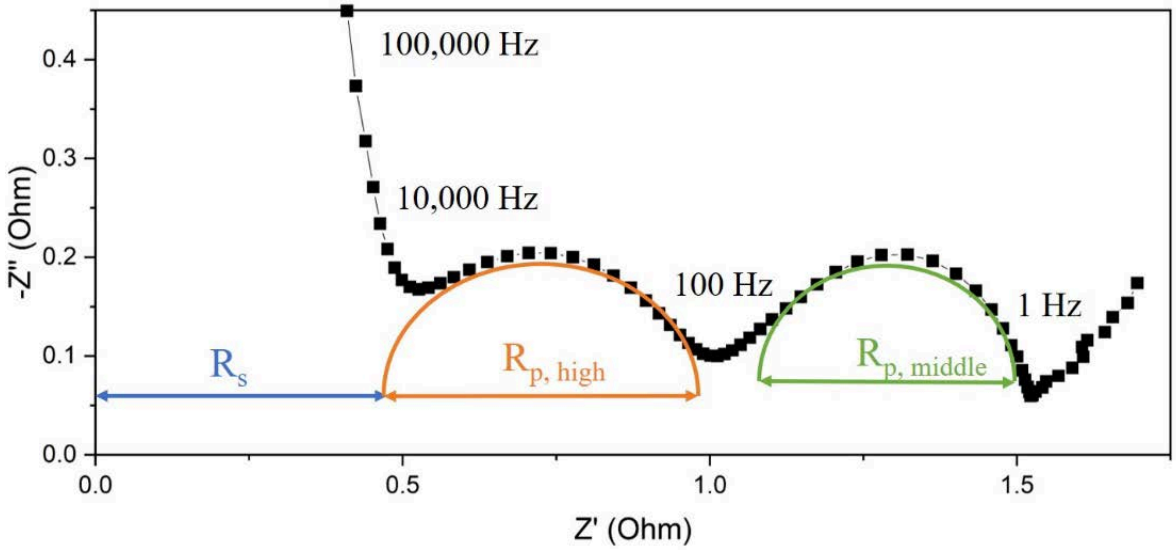

Figure 8. EIS fitting result from a parametric test at 800 °C (10% H_2) of a cell with an LSM 85-90 cathode on a 100-μm-thick electrolyte. R_s=0.41 Ω, $R_{p,\,high}$=0.63 Ω, $R_{p,\,m}$=0.47 Ω.

The spectrum in Figure 8 shows a sharp rise in $|-Z''|$ at high frequencies (the left side of the plot). Most of the EIS spectra measured in this project exhibited this "high-frequency tail." Late in the project, we were able to significantly reduce this effect by arranging the leads that ran from the bottom of the text fixture to the electrochemical workstation to be several inches apart

from each other. This indicates that the high-frequency tail was an artifact of electromagnetic interference between these (unshielded) portions of the leads. The effects of the high-frequency tail on the analysis of the EIS data will be addressed in the section on DRT analysis in the Findings.

Interpretation of EIS measurements: Distribution of relaxation times (DRT) analysis. Due to the relatively poor resolution of impedance spectroscopy in a small-impedance system such as the SOFC button cell studied here, some electrochemical processes overlap in the frequency domain. This increases the difficulty in fitting an equivalent circuit. By calculating the distribution of relaxation times (DRT), each process is determined by its intrinsic time constant [22]. In principle, each peak in a DRT analysis represents an electrochemical process, and the peak area indicates the resistance loss but cannot be quantified. The relation between the impedance at a certain frequency $Z(\omega_i)$ and the probability density function of relaxation times $\gamma(\tau)$ is shown as follows:

$$Z(\omega_i) = R_s + R_p \int_{-\infty}^{\infty} \frac{\gamma(\tau)}{1+i\omega_i\tau} dln\tau \quad (2)$$

where R_s is the ohmic resistance of the sample, and R_p is the polarization resistance (high frequency cut-off resistance). Furthermore, $\gamma(\tau)$ is a normalized function:

$$\int_{-\infty}^{\infty} \gamma(\tau) dln\tau = 1 \quad (3)$$

Dierickx et al. [23] suggested that smaller values of the regularization parameter, λ, which controls the smoothness of DRT results, provided a smaller deviation between the DRT fit and the experimental data, but introduced more peaks into the system to fit the impedance data. These additional peaks have no physical meanings in the investigated system but only mathematically reduce the deviation. As there is no definitive method to obtain a universally valid λ, an optimal value strongly depends on the system and measurement, and a value that is smaller than 10^{-2} is often accepted [20].

In our study, DRT analysis was accomplished using the DRT Tools software (Hong Kong University of Science and Technology, Hong Kong, China) [24]. The parameters were chosen as follows:

- Discretization method: Gaussian,
- Regularization parameter, λ: 10^{-3},
- Regularization derivative: 1st-order,
- Radial basis function (RBF) shape control: Coefficient to full width at half maximum (FWHM) – 0.5.

Cell and electrode ASR. Three methods were used to obtain the area specific resistance of the cell as a function of time, $ASR(t)$. From the readings of cell output voltage $V(t)$ during a durability test,[5] an $ASR_{DC}(t)$ can be computed as

$$ASR_{DC}(t) = \frac{V_{OC}(t) - V(t)}{J} \quad (4)$$

where the value of $V_{OC}(t)$ was taken to be the last measured reading of open-circuit voltage. (Open-circuit voltage decreased slightly during durability testing, typically from near 1.09 V to about 1.08 V at 1,000 °C, and from 1.08 V to about 1.05 V at 900 °C.)

[5] Equation (4) cannot be used to determine ASR for aging tests because current density $J = 0$ during aging tests.

The equivalent circuit fits of Nyquist plots from EIS measurements can also yield estimates of the cell's ASR. Unlike ASR_{DC}, this allows ASR to be estimated during aging tests, from the EIS spectra taken during the parametric tests and every 24 during the aging test.[5] Some of the Nyquist plots showed only a single broad arc; others exhibited two distinct arcs.[6] Figure 9 and equations 3a and 3b show how single-semicircle (left) or two-semicircle fits (right) can be used to estimate a cell's ASR as ASR_{EIS} [25].

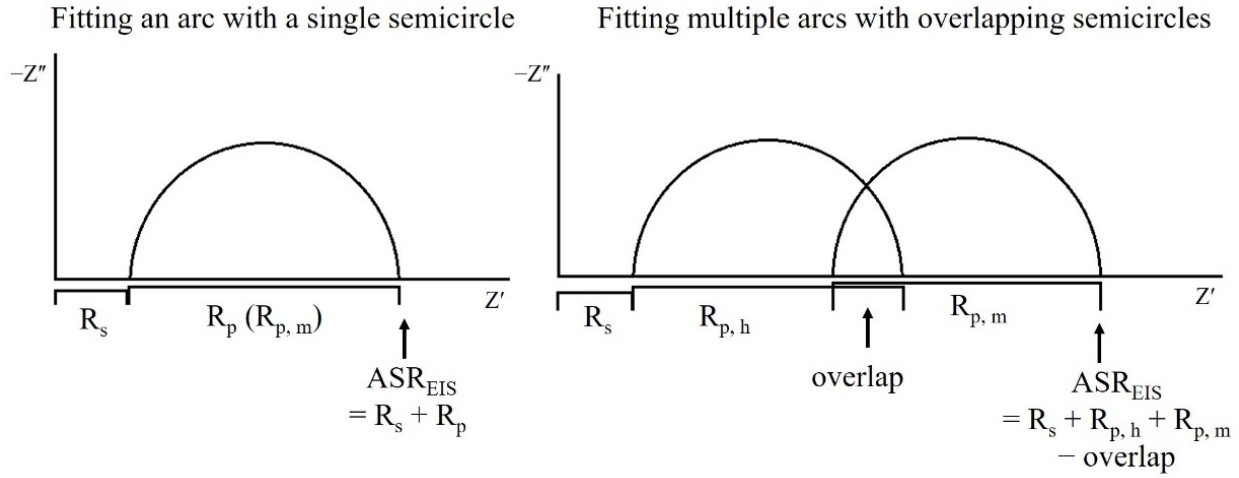

Figure 9. Single-arc (left) and two-arc fitting (right) [44] (Madeleine McAllister, CWRU).

$$\text{One semicircle: } ASR_{\text{EIS}} = R_{\text{s}} + R_{\text{p}} \tag{5a}$$

$$\text{Two semicircles: } ASR_{\text{EIS}} = R_{\text{s}} + R_{\text{p,h}} + R_{\text{p,m}} - overlap = R_{\text{s,m}} + R_{\text{p,m}} \tag{5b}$$

Figure 10 shows examples of actual one-semicircle (left) and two-semicircle fits (right). In the single-semicircle fit, a faint shoulder at the base of the high-frequency tail indicates that another arc is probably included in R_s. This shoulder may result from a similar process as $R_{p,h}$ in the two-semicircle fit, but it is hard to separate that arc from R_s when the high-frequency tail is present. At the same time, since both anode and cathode contain YSZ (which conducts oxygen ions), it is also difficult to separate the contributions of anodic YSZ, cathodic YSZ, and electrolyte YSZ from R_s. In previous work, our group assigned the higher-frequency arc to anodic processes [26] and cathodic processes to lower-frequency arcs (< 10^3 Hz, Table 4.1), compatible with other studies [27].

The overlap shown in Figures 9 and 10 can be calculated as $overlap = R_{s,h} + R_{p,h} - R_{s,m}$, where $R_{s,m}$ is the offset of the left edge of the medium-frequency semicircle. Therefore the total ASR_{EIS} fitting can be expressed as $ASR_{EIS} = R_{s,m} + R_{p,m}$. As shown in Figure 9 (right), in a two-semicircle fit, $R_{s,m}$ does not correspond to an actual series resistance in the equivalent circuit model. It is a consequence of the limitation of our fitting software, which can only fit one semicircle at a time.

The third way that cell ASR can be computed is from the LSV sweeps taken daily during extended testing (durability or aging). Equation 4 (for ASR_{DC}) is based on an assumption that the voltage varies linearly with the current. However, in practice, the *I-V* curve is not strictly linear

[6] Any arc on a Nyquist plot could result from multiple electrochemical processes with overlapping relaxation times, but without distinct minima or at least inflection points in the arc, it is usually not possible to fit multiple semicircles unambiguously to any single arc in an EIS spectrum.

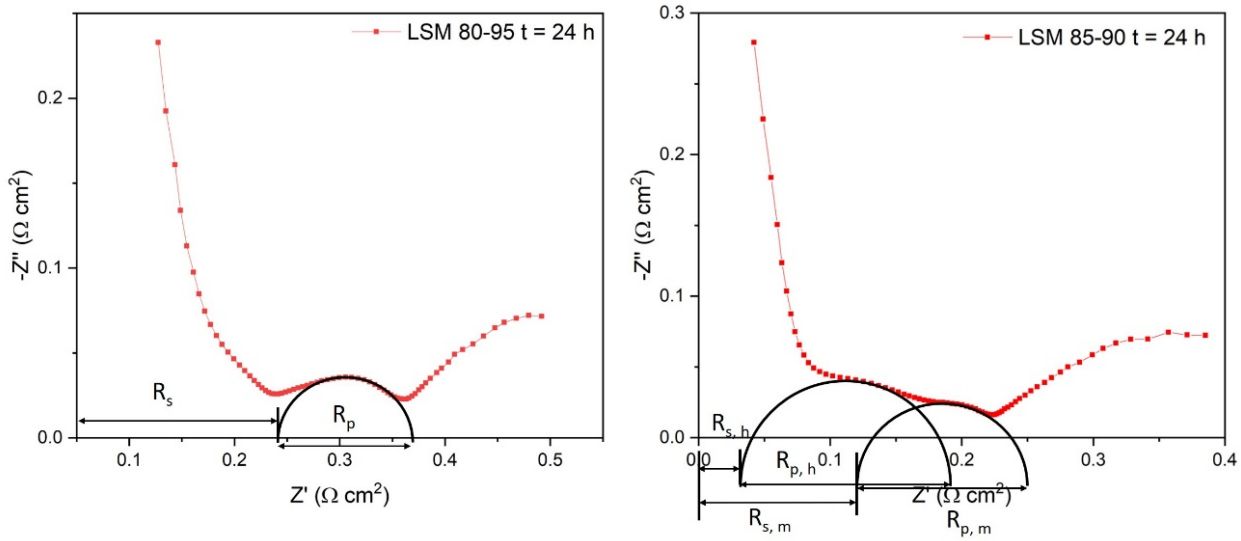

Figure 10. Left: Single-arc fitting from a cell with an LSM 80-95 cathode tested at 900 °C, 760 mA cm $^{-2}$, 10% O_2 at t = 24 h. R_s = 0.217 Ω cm^2, R_p = 0.167 Ω cm^2. Right: two-arc fitting from a cell with an LSM 85-90 cathode tested at 1,000 °C, 760 mA cm $^{-2}$ in air at t = 24 h. R_s = 0.029 Ω cm^2, $R_{p,h}$ = 0.165 Ω cm^2, $R_{s,m}$ = 0.142 Ω cm^2, $R_{p,m}$ = 0.093 Ω cm^2.

(Fig. 11), so the ASR actually varies with current density. (The nonlinearity of the *I-V* curves of high-temperature fuel cells like SOFCs is less pronounced than for lower-temperature fuel cells, because lower-temperature cells have higher activation polarization losses that give them more pronounced, concave-upward curvature at low current.) Another method for calculating ASR as a function of current density is from the tangent of the *I-V* curve:

$$ASR_{\mathrm{LSV}} = \frac{dV_J}{dJ} \qquad (6)$$

where V_j is the voltage at current density J. Figure 11 shows one example of how ASR_{DC} and ASR_{LSV} both differ from each other and vary independently with current density, in a single *I-V* curve from a cell with an LSM 80-95 cathode in air at 1,000 °C. In this work, ASR_{LSV} was computed by performing a linear fit to the linear region of the *I-V* curve.

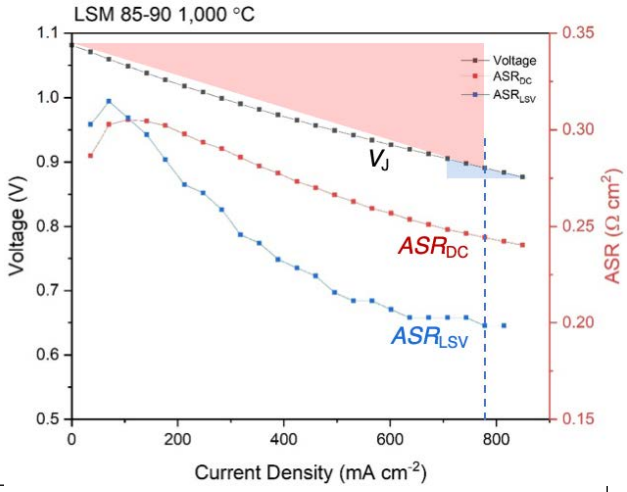

Figure 11. Comparison of ASR_{DC} (eq. 4, red) and ASR_{LSV} (eq. 6, blue). Slopes of the triangles give ASR values computed at 0.775 A cm^{-2}.

The anodes of all cells tested in this and the prior project were nominally identical. The electrolytes were all made of 8YSZ; all were 100 µm thick, except the first batch of cells with LSM 85-90 cathodes (tested in the prior project) which were 200 µm thick. The electrolyte makes a significant contribution to the cell ASR (mainly in the series resistance R_s) that depends on its thickness, and also its temperature. As an approximate way to exclude the electrolyte ASR (and its dependence on thickness and temperature) from the total cell ASR, and to be able to focus on ASR attributable mainly to the electrodes, literature data [28] for the conductivity of 8YSZ versus

temperature were used to compute the area specific resistance of the electrolyte, $ASR_{e'lyte}$ from its thickness ℓ and conductivity $\sigma(T)$ at the test temperature:

$$ASR_{e\prime lyte} = \frac{\ell}{\sigma(T)} \quad (7)$$

Table 1 gives the values of $ASR_{e'lyte}$ relevant to this work. To obtain estimated values of ASR of the electrodes $ASR_{e'ode}$, $ASR_{e'lyte}$ was subtracted from experimental values of total cell ASR:

$$ASR_{e\prime ode} = ASR - ASR_{e\prime lyte} \quad (8)$$

where ASR here represents any of the three versions of total cell ASR (ASR_{DC}, ASR_{EIS}, or ASR_{LSV}) as expressed in equations (4)–(6).

	900 °C	1,000 °C
100 μm	0.22 Ω cm^2	0.11 Ω cm^2
200 μm	0.44 Ω cm^2	0.23 Ω cm^2

Table 1. Estimated electrolyte area specific resistance at different temperatures and thicknesses.

Microstructural sample preparation and examination. After testing, cells were cut off of the cell support tube using a low-speed saw (Buehler Isomet) with a diamond-impregnated blade and cleaned with 95% ethanol. The cell was vacuum-infiltrated with an epoxy mounting medium (Buehler) with the aim of filling the open pores in the anode and cathode. The mounted cell was then cured at room temperature for at least 24 hours. Mounted specimens were sectioned with the cross section of the cell at two orthogonal surfaces of the mount (Fig. 12). Mounts were ground with abrasive silicon carbide papers (P400, P800, P1200) and polished with diamond suspensions (3 μm, 1 μm, 0.25 μm).

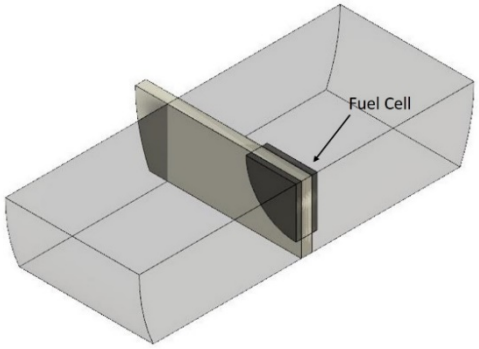

Figure 12. Illustration of mounted and sections SOFC button cell.

The polished specimens were first mounted on an SEM stub (using conductive carbon tape) and sputter-coated with 4–5 nm of palladium. Microstructure analysis (Helios NanoLab 650 SEM with EDS system) was carried out in the CWRU's Swagelok Center for Surface Analysis of Materials (SCSAM). Secondary electron (SE) images were usually collected at 5 kV, and backscattered electron (BSE) images were collected at 15 or 20 kV. EDS was collected at 20 kV, with beam current to give ~30% dead time, typically 0.8 nA. Color EDS maps (Mn: green; Zr: blue; La: red) were superimposed on the corresponding image, enabling grains and regions to be identified as either LSM (yellow), porosity (black), YSZ (blue), or manganese oxide (MnO_x, green).

Backscattered electron images amplify the differences in average atomic number between phases with different elemental compositions. ImageJ software was used to choose ranges of gray-scale in each BSE image that most closely corresponded to pores (darkest regions), YSZ (intermediate gray), and LSM (bright gray). Threshold levels had to be determined independently for each image depending on its brightness and contrast. The pixel fraction of pores and LSM was taken to be the volume fraction of those phases [29], and the volume fraction of YSZ was taken to be the remainder. To estimate the uncertainties in the pore and LSM volume fractions, "under" and "over" estimates were also measured, by altering the threshold gray level by 4-10 units (out of 255). The uncertainties in the YSZ fractions are the sum of the uncertainties in the pore and LSM fractions. Images with low contrast needed larger "under" and "over" ranges.

Manganese oxides appear as dark gray in BSE images, but in individual images it was difficult to find a unique range of grayscale that reliably distinguished MnO_x from both pores and YSZ. Identification of MnO_x particles therefore relied on identification of green regions in the EDS maps that likewise corresponded to discretely darker-gray regions in BSE images.

Findings

During the course of the project, 17 tests were undertaken: four on cells with LSM 85-90 cathodes, seven on cells with LSM 80-95 cathodes, four on cells with LSM 80-98 cathodes, and three on cells with composition D cathodes. Full results of all of these tests are presented in the thesis of Chenxin Deng [20], whose graduate assistantship was supported by this project.

Six of these tests were significant either for their length, their operating conditions (e.g. for comparing operation in air versus low oxygen, or aging versus durability testing) or for enabling comparisons among the different cathode compositions. The results of these tests will be discussed in detail in this section.

LSM 85-90 cathode, 1,000 °C, 0.76 A cm^{-2}, air, 1,008 h. The Nyquist plots (Figs. 13; 14, left) despite showing the high-frequency tail (discussed above), also show clear evidence of at least two arcs. This enabled two-arc equivalent circuits to be fit, giving the time-dependence of the individual ASR components of $R_{s,h}$, $R_{p,m}$, $R_{p,h}$ and of ASR_{EIS} for the entire test (Figs. 10, 13). The unusual length of this test permitted three rounds of parametric testing to be carried out: at 0, 504, and 1,008 h of testing (Fig. 13), with the cell exhibiting normal behavior at all three of these stages of the durability test: impedance (both Z' and Z'') increasing with decreasing temperature, and with increasing time of durability testing. Table 2 gives the results of equivalent circuit fitting for those parametric tests, as well as for EIS measurements taken every ~200 h at 1,000 °C in air during durability testing.

During durability testing at 1,000 °C and current density of 760 mA cm^{-2}, this cell exhibited frequent voltage drops beginning at 430 h and continuing until the intended duration of the test of 504 h (21 days) (Fig. 15, left). Between voltage drops, the cell operating voltage was normal, so the cell was held at 1,000 ℃ for about 144 h (6 days) at OCV under the chosen anode and cathode atmospheres. When the current was reapplied, the voltage drops did not reappear, and the cell operated another 360 h (15 days). When the test was ended after 1,008 h[7] (42 days) at temperature, including 864 h[8] (36 days) under aggressive current density, it was showing no signs of imminent failure. This was the longest test completed in this (and the preceding) project.

From 0 to 430 h, this cell exhibited normal behavior with a moderate degradation rate (for this study) of 38.6% per kh (as measured from the slope of total cell ASR_{DC} versus time; see Figure 35 below). During the second 360 h of normal output, its degradation rate was 23.3% per kh, relatively low for this work. Over the entire test, with total cell ASR_{DC} of 0.248 and 0.303 Ω cm^2 at t=0 and 1,000 h, respectively, the degradation rate was 22.2% per kh.

Figure 14 shows the results of EIS measurements over the course of this test. Values of ASR_{EIS} (Table 2) versus time were in excellent agreement with the values of ASR_{DC} (Fig. 35). Linear fits to all of the individual ASR components (Fig. 14, right) show gradual increases with time. The component $R_{p,h}$ was the single largest contribution to ASR_{EIS}, 60%–64% throughout the test, and increased more rapidy with time than either $R_{s,h}$ *or* $R_{p,m}$. Table 2 includes numerical values

[7] Throughout this report, the given test durations do not include the burn-in phase (24 h of operation under load).

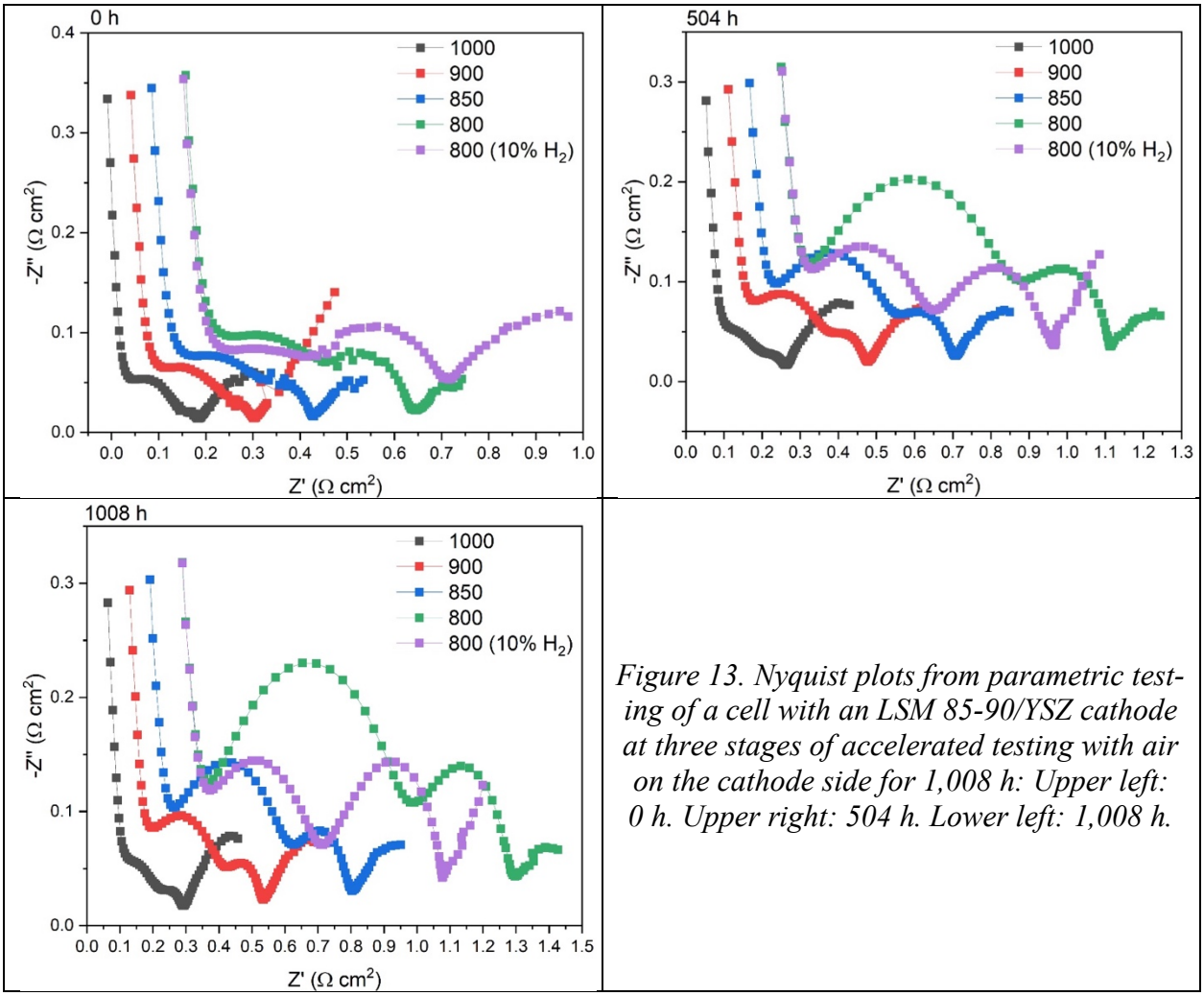

Figure 13. Nyquist plots from parametric testing of a cell with an LSM 85-90/YSZ cathode at three stages of accelerated testing with air on the cathode side for 1,008 h: Upper left: 0 h. Upper right: 504 h. Lower left: 1,008 h.

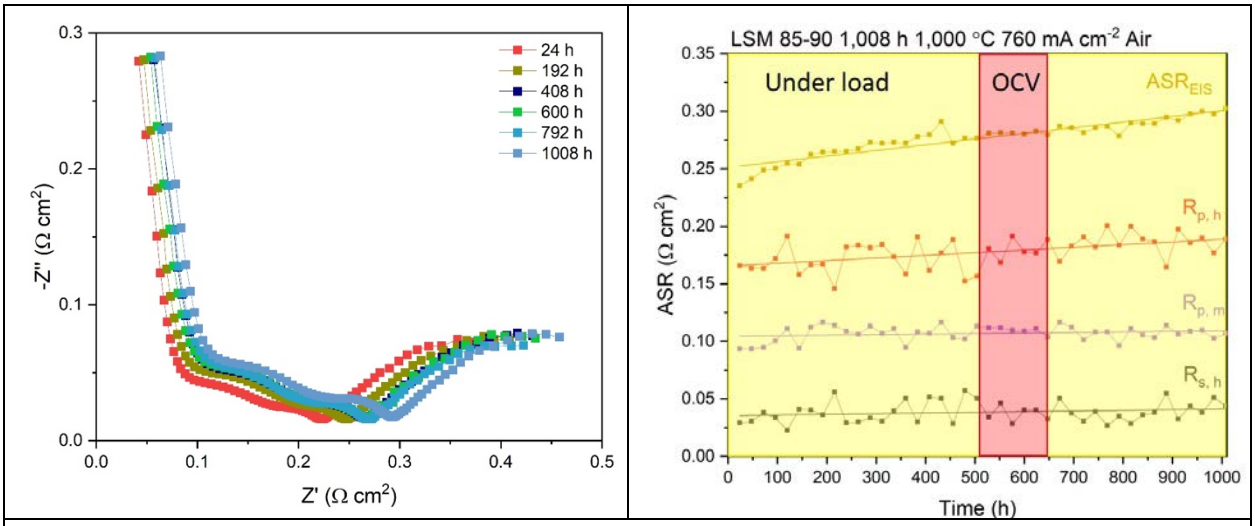

Figure 14. EIS results from a cell with an LSM 85-90 cathode: durability test at 1,000 °C in air at 0.76 A cm^{-2} for 1,008 h. Left: Nyquist plots at ~200-h intervals. Right: Results of equivalent circuit fits to EIS data every 24 h. See text for definitions of $R_{s,h}$, $R_{p,m}$, $R_{p,h}$, and ASR_{EIS}. Straight lines are linear best fits to each set of data.

from these fits every ~200 h. Results from DRT analysis will be discussed below.

Test	T, °C	$R_{s,h}$[8], Ω cm^2	$R_{p,h}$, Ω cm^2	$R_{s,m}$, Ω cm^2	$R_{p,m}$, Ω cm^2	ASR_{EIS}, Ω cm^2
LSM 85-90, air, t=0 (before durability testing)	1,000	–0.008	0.158	0.107	0.092	0.199
	900	0.007	0.266	0.228	0.077	0.305
	850	0.052	0.314	0.316	0.112	0.428
	800	0.076	0.453	0.445	0.195	0.640
	800 (10% H_2)	0.034	0.536	0.385	0.359	0.744
LSM 85-90, air, t=504 h (middle of durability testing)	1,000	0.040	0.168	0.167	0.110	0.276
	900	0.095	0.308	0.341	0.141	0.483
	850	0.170	0.409	0.518	0.194	0.711
	800	0.267	0.641	0.876	0.241	1.117
	800 (10% H_2)	0.234	0.450	0.662	0.298	0.961
LSM 85-90, air, t=1,008 h (end of durability testing)	1,000	0.025	0.216	0.195	0.108	0.303
	900	0.117	0.322	0.397	0.141	0.539
	850	0.201	0.444	0.607	0.196	0.803
	800	0.321	0.696	0.983	0.306	1.290
	800 (10% H_2)	0.280	0.455	0.756	0.332	1.087
LSM 85-90, during durability testing at 1,000 °C, air, 0.76 A cm^{-2}.	t, h	$R_{s,h}$, Ω cm^2	$R_{p,h}$, Ω cm^2	$R_{s,m}$, Ω cm^2	$R_{p,m}$, Ω cm^2	ASR_{EIS}, Ω cm^2
	24	0.029	0.166	0.142	0.093	0.235
	192	0.036	0.167	0.148	0.117	0.264
	408	0.052	0.161	0.172	0.107	0.279
	600	0.040	0.178	0.171	0.109	0.280
	792	0.035	0.183	0.182	0.096	0.278
	1,008	0.044	0.189	0.196	0.107	0.303

Table 2. Results for equivalent circuit fitting of a cell with an LSM 85-90 cathode, tested at 1,000 °C, air, 0.76 A cm^{-2}, 1,008 h: from parametric testing at 0, 504, and 1,008 h; and from selected EIS measurements every ~200 h. All runs were fit with two semicircles. For parametric runs, $1.51\times10^{-5} < \chi^2 < 2.87\times10^{-4}$.

[8] Due to the limitation of NOVA software, only one arc can be fit at a time. Hence, the $R_{s,h}$ is treated as the R_s of the cell and ASR is the sum of $R_{s,m}$ and $R_{p,m}$.

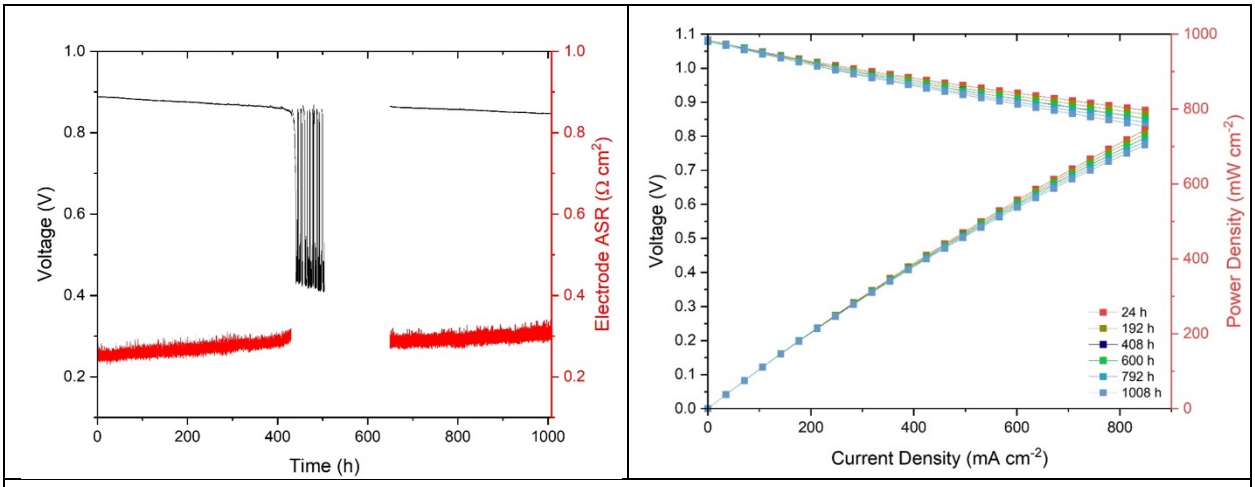

Figure 15. Durability test of a cell with an LSM 85-90 cathode, 1,000 °C, air, 0.76 A cm^{-2}, 1,008 h. Left: Voltage and electrode ASR_{DC} vs. time. Right: LSV sweeps at ~200-h intervals.

Figure 16 shows a post-test SEM (BSE) image, and elemental EDS maps (La, Zr, and Mn only) superimposed on the SE image, across the entire cathode of this cell. Backscattered electron imaging provides higher contrast between phases based on their atomic number (*Z* contrast). As a result, LSM (highest average *Z*) is the brightest phase, 8YSZ is intermediate gray, manganese oxide (MnO_x) is dark gray, and pores are black. The boundaries between the cathode (which contains both 8YSZ and LSM), the electrolyte (just YSZ), and the cathode current collector (just LSM) can therefore be distinguished.

It is sometimes difficult to distinguish MnO_x from pores in the grayscale image, but EDS mapping is able to distinguish MnO_x (green) from LSM (yellow-orange), YSZ (blue), and pores (black). White circles indicate the most conspicuous MnO_x grains, corresponding to distinct green regions in the EDS map and dark gray regions in the BSE image. Red circles tentatively indicate other possible MnO_x particles. SEM/EDS analysis counts x-rays emerging from a depth of micrometers below the plane of polish, more so at high accelerating voltages of the electron beam. (Whereas the secondary electron images were usually collected at 15 keV, the EDXS spectra were collected at 20 keV.) Therefore SEM/EDXS maps show indistinct colors, and relatively blurry boundaries between phases: the thickness of typical SEM specimens increases the likelihood that there are grains of different composition hidden below the plane of polish, adding x-rays from other elements to the maps of the grains visible in the image.

In contrast, EDXS maps obtained from TEM images (e.g. Fig. 17) of the prior project typically show more distinct colors of different phases, and sharper boundaries between phases. That is because TEM foils must be much thinner than SEM specimens, as the electron beam must pass through TEM specimens to form the image. This enabled even small MnO_x particles to be identified with a high degree of confidence.

Despite these caveats, Figure 16 shows that MnO_x grains are common in the all-LSM CCC, but scarcer in the YSZ/LSM cathode. Furthermore, the MnO_x grains that are visible in the cathode are within about 2 µm of the cathode/electrolyte interface, in a total cathode thickness of 14 µm. The only other definitive MnO_x grain "in" the cathode is at the cathode/CCC interface. Otherwise, only tentative identifications of MnO_x occur farther than 2 µm from the electrolyte.

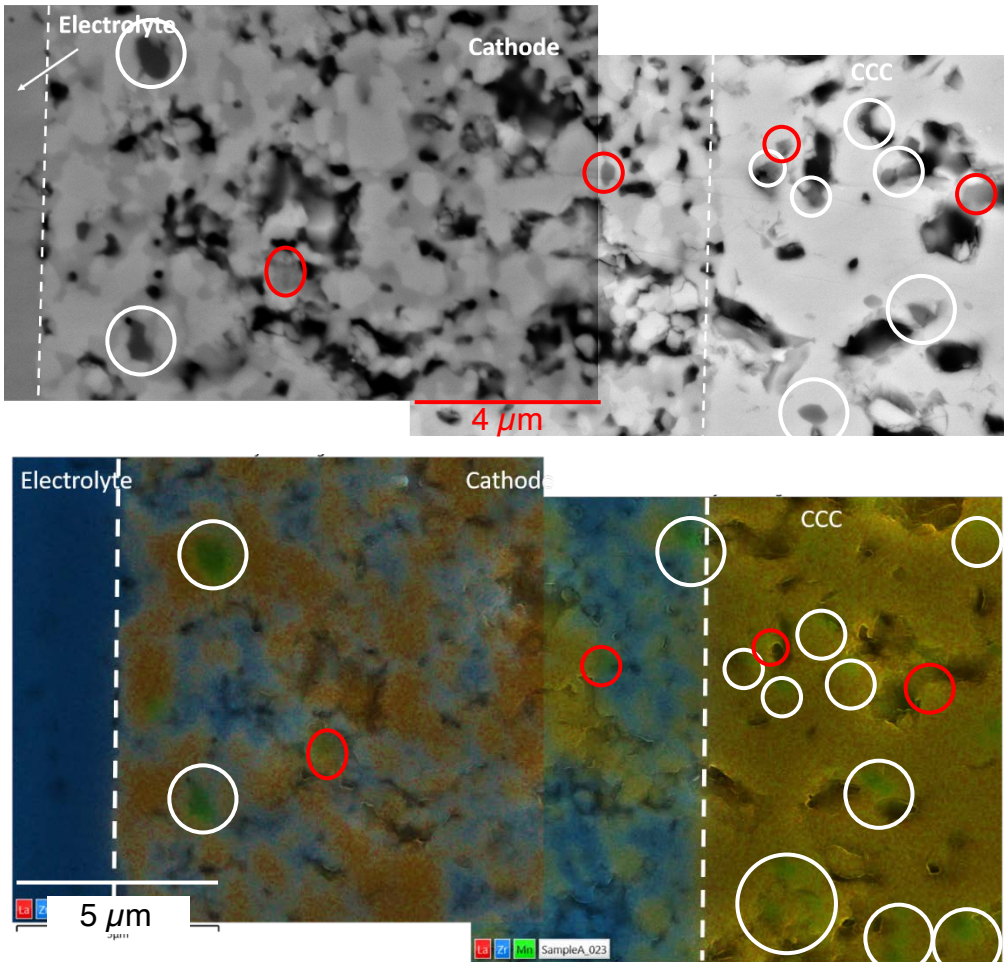

Figure 16. Spliced images of an LSM 85-90 cathode, after testing at 1,000 °C at 0.76 A cm^{-2} in air for 1,008 h. From left to right: electrolyte, cathode, cathode current collector (CCC). Top: BSE images. Bottom: EDXS maps (La, Zr, Mn). YSZ appears blue; LSM, yellow or yellow-orange; pores, black; MnO_x, green. White circles indicate where BSE and EDS images support identification of MnO_x particles; red circles indicate more tentative identification of MnO_x.

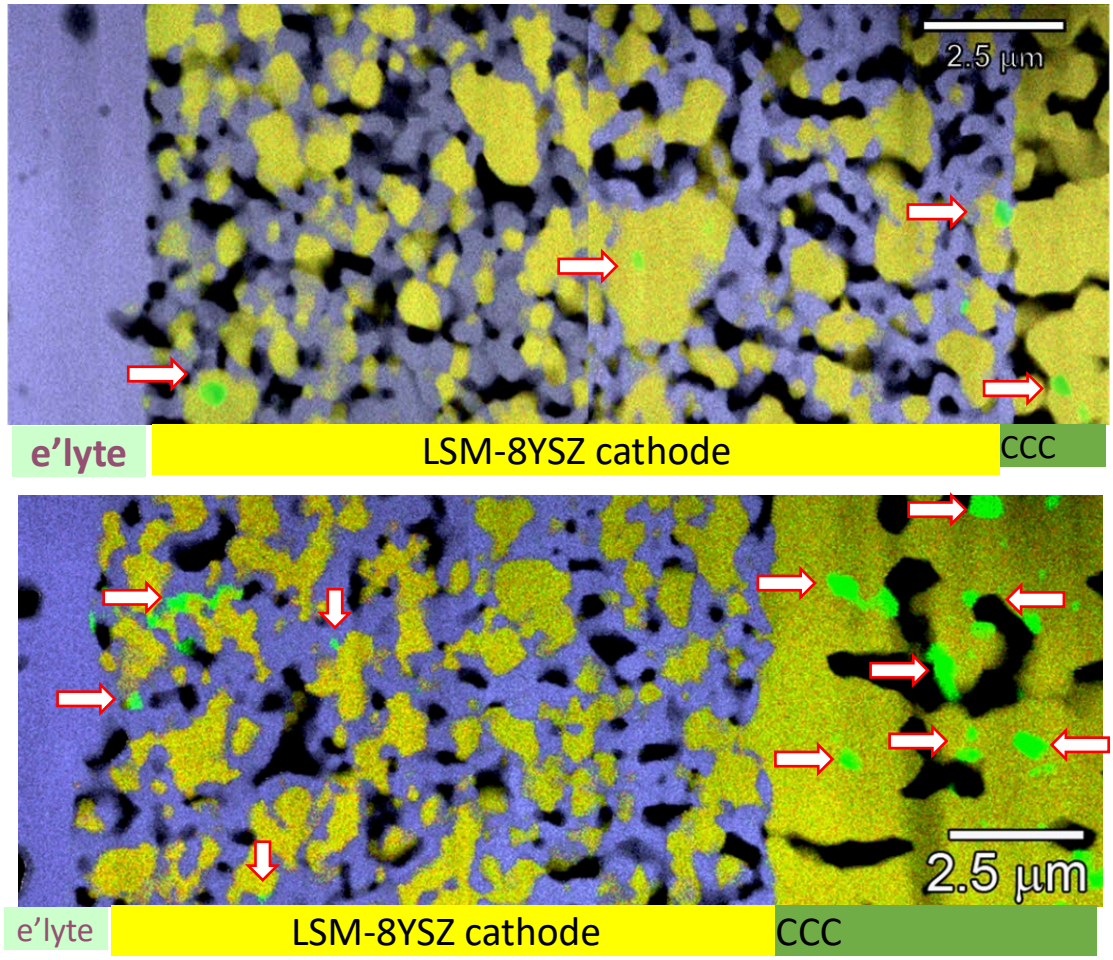

Figure 17. Spliced TEM/EDXS maps of cells with LSM 85-90 cathodes: as received (top) and after 493 h of accelerated testing in air (bottom). Left to right: electrolyte, cathode, cathode current collector (CCC). YSZ is blue; LSM, yellow; pores, black; MnO_x, green (arrows) [30].

Figures 18 and 19 show, respectively, the thresholding of the left side (cathode/electrolyte interface) and the right side (cathode/CCC interface) of Figure 16, as described in the Approaches section. At the cathode/electrolyte interface: pores (24.9±3.6)%; LSM (41.6±6.3)%; YSZ 33.5%; at the cathode/CCC interface: pores (21.8±2.7)%; LSM (29.1±11.8)%; YSZ 49.1%. These results agreed between the cathode/electrolyte and cathode/CCC interfaces, in light of the uncertainties. The values at the cathode/electrolyte interface (Fig. 18) are in excellent agreement with phase fractions determined using 3-D reconstruction on an as-received cell with LSM 85-90 cathode on a "thin" (100 µm) substrate in the previous project — (23±3)% pores, (41±3)% LSM, and (35±3)% YSZ. The somewhat over-exposed image from the cathode/CCC interface (Figure 19) resulted in high uncertainties in the LSM fraction, but within these uncertainties the values of the phases also agree with the fractions in the as-received specimen as determined by 3DR.

These observations are consistent with previous observations of cells with LSM 85-90 cathodes. Figure 17 shows TEM/EDS images of an LSM 85-90 cathode as received (top) and after 493 h of testing in the same conditions as the cell in Figure 16. Arrows mark MnO_x grains. In the as-received cell, MnO_x grains are visible at random in the cathode and the CCC. In the tested cell, MnO_x grains are distributed randomly in the CCC, whereas the MnO_x grains in the cathode are

aggregated within 2 µm of the cathode/electrolyte interface, except for a couple of tiny ones (marked by vertical arrows). With regard to feature sizes as well as MnO_x distribution, the microstructures of cells tested for 1,008 h (Fig. 16) and 493 h (Fig. 17) are very similar.

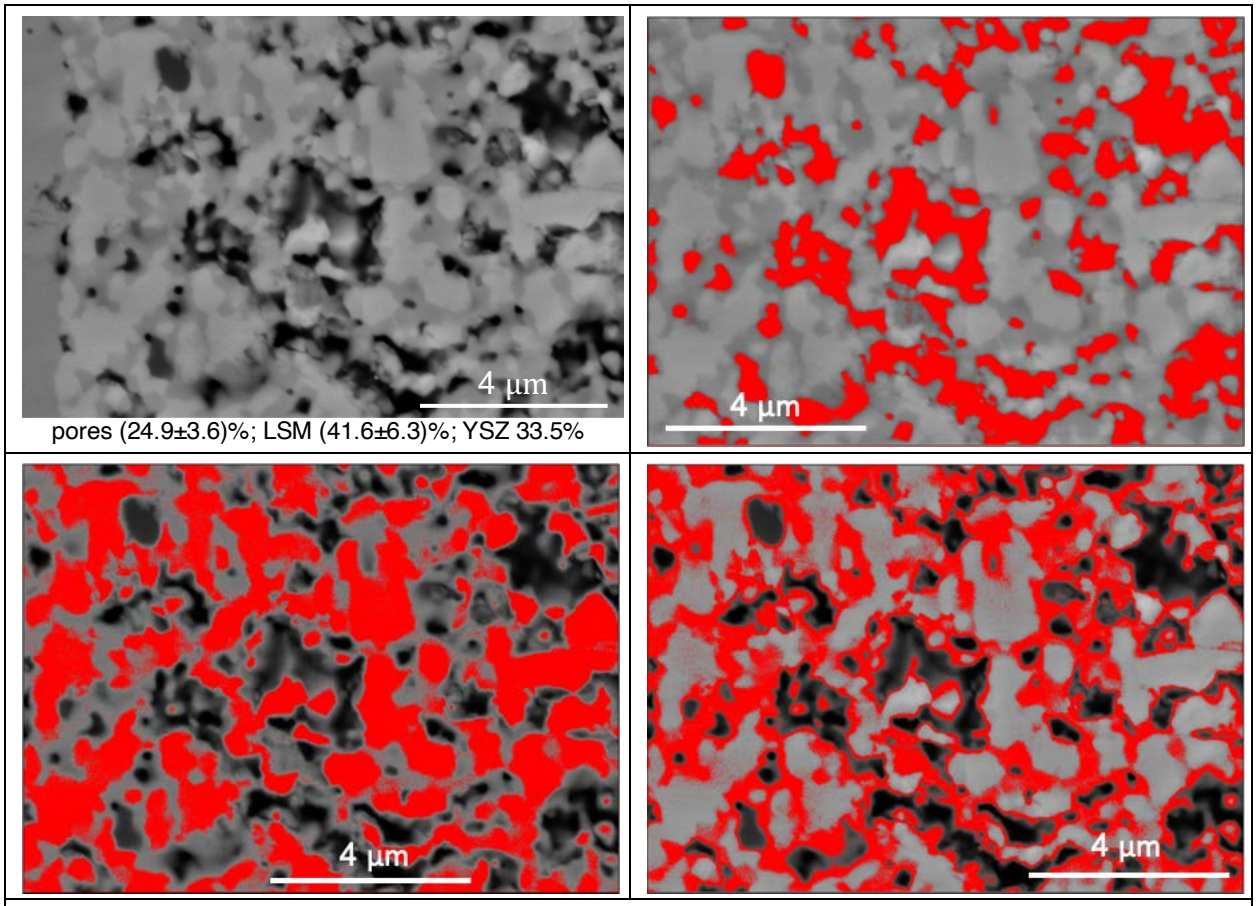

Figure 18. Estimation of phase fractions of the cathode-electrolyte interface of Figure 16. Upper left: original BSE image; volume fractions equal pixel fractions in the thresholded images. Upper right: pores in red (gray level 0–94). Lower left: LSM in red (133–255). Lower right: YSZ in red (95–132).

On both the thin and thick electrolytes, the porosity of LSM 85-90 cathodes was lower than for the other cathode formulations studied in this work (especially on the thick electrolytes). This suggests that LSM 85-90 in general is more prone to densification during firing, as well as during operation under aggressive conditions (here, high temperature and current density). Both the 493-h and 1,008-h microstructures (Figs. 16 top, 17 bottom) exhibit significantly less porosity at both the cathode/electrolyte and the cathode/CCC interfaces. This microstructural effect could be expected to be a significant source of performance degradation, by limiting the supply of oxygen to the electrolyte mainly to that which can arrive by ionic conduction (rather than percolation). Still, the cell shown in Figure 16 was by several metrics (length; low ASR) the most successful test run in this project and its predecessor.

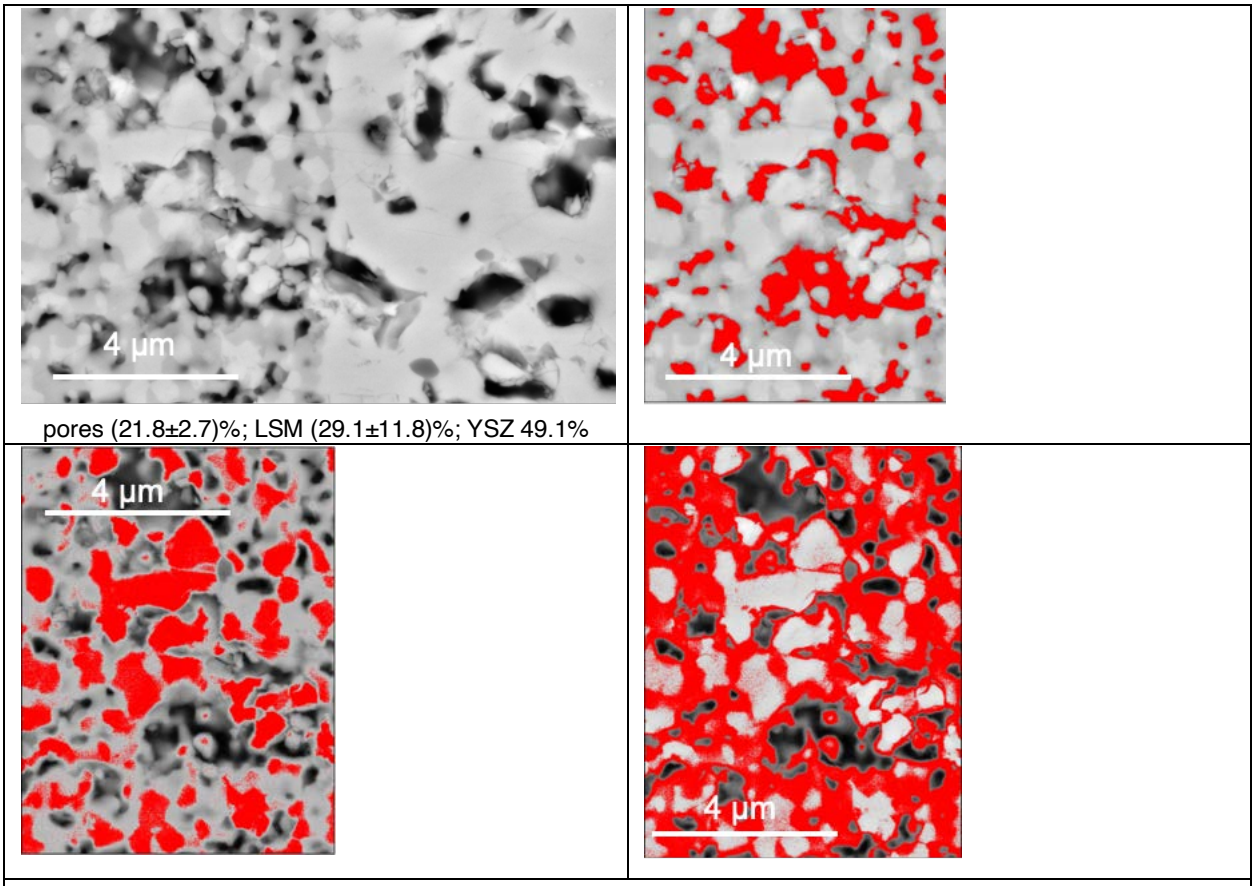

Figure 19. Estimation of phase fractions of the cathode-CCC interface of Figure 16. Upper left: original BSE image; volume fractions equal pixel fractions in the thresholded images. Upper right: pores in red (gray level 0–137). Lower left: LSM in red (200–255). Lower right: YSZ in red (138–199).

Aging tests: LSM 85-90, 1,000 °C, air, 209 h; LSM 80-98, 900 °C, 10% O_2, 500 h. Two extended aging tests were completed with different LSM compositions, temperatures, and cathode atmospheres: LSM 85-90, 1,000 °C, air; and LSM 80-98, 900 °C, 10% O_2 (balance nitrogen). The purpose of aging tests is to isolate the effects of temperature and atmosphere, from the additional effects of active conversion of chemical energy to electricity during operation. The effect of LSM composition is expected to be minimal in tests where the cell remains at OCV: at zero current the conductivity and catalytic effectiveness of the cathode (or the other active components of the cell) do not come into play.

Before the start of the aging tests, the parametric tests for both cells (Fig. 20) showed expected dependences on temperature and cathode atmosphere (cell ASR rising with decreasing temperature and with decreasing-p_{O_2}). Results of equivalent-circuit fits to the parametric tests (Table 3) support these trends for all circuit components and temperatures in most cases.

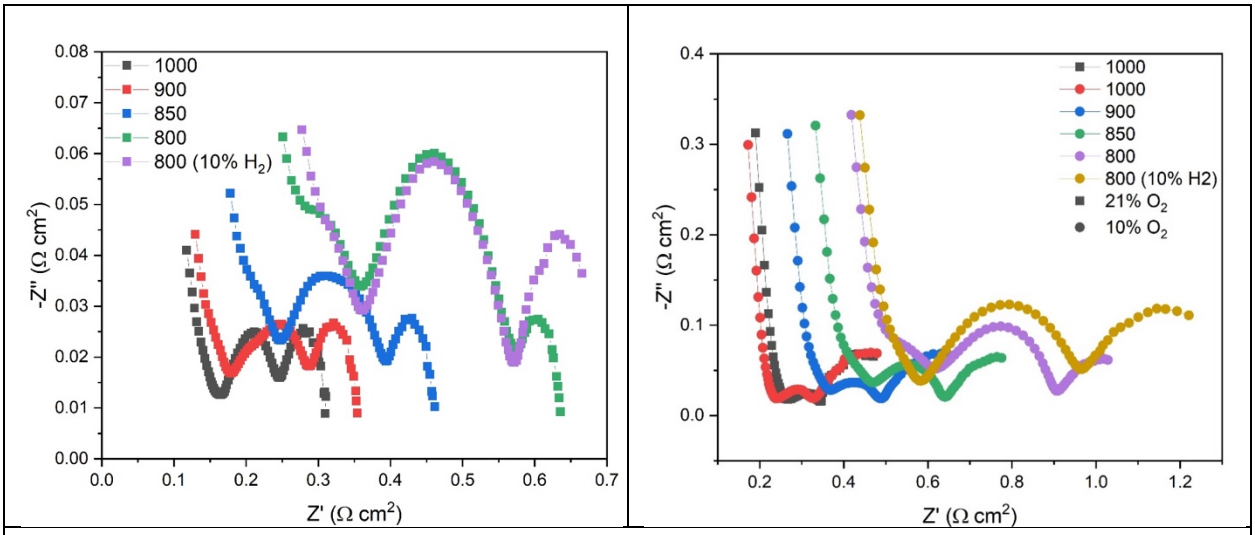

Figure 20. Nyquist plots from parametric tests at t=0 h prior to aging tests. Left: a cell with an LSM 85-90 cathode, in air. Right: a cell with an LSM 80-98 cathode, p_{O_2} = 0.10 (with one reading at 1,000 °C in air).

Test	*T*, °C	$R_{s,h}$,[9] Ω cm^2	$R_{p,h}$, Ω cm^2	$R_{s,m}$, Ω cm^2	$R_{p,m}$, Ω cm^2	ASR_{EIS}, Ω cm^2
LSM 85-90, air (before 209 h of aging at 1,000 °C)	1000	—	—	0.162	0.097	0.259
	900	0.113	0.071	0.185	0.122	0.307
	850	0.131	0.132	0.225	0.163	0.389
	800	0.189	0.202	0.339	0.239	0.578
	800 (10% H_2)	0.159	0.230	0.354	0.212	0.566
LSM 80-98, 10% O_2 (with one reading at 1,000 °C in air) (before 500 h of aging at 900 °C)	1,000 (air)	—	—	0.264	0.090	0.355
	1,000	—	—	0.245	0.089	0.334
	900	—	—	0.334	0.180	0.515
	850	—	—	0.467	0.182	0.648
	800	0.221	0.458	0.635	0.275	0.910
	800 (10% H_2)	—	—	0.587	0.401	0.988

Table 3. Results for equivalent circuit fitting of parametric tests at t = 0, prior to aging tests of two cells: one with an LSM 85-90 cathode in air, and one with an LSM 80-98 cell in low oxygen. For all runs, $7.10\times10^{-7} < \chi^2 < 1.15\times10^{-5}$. Runs for which no values are given for $R_{s,h}$ and $R_{p,h}$ were fit with a single semicircle; all others were fit with two semicircles.

Figure 21 shows how the open-circuit voltage (OCV) of these cells varied with time. The test in air (Fig. 21, left), despite an unexplained drop in OCV from 50 to 100 h, overall showed no

[9] Due to the limitation of NOVA software, only one arc can be fit at a time. Hence, the $R_{s,h}$ is treated as the R_s of the cell and ASR is the sum of $R_{s,m}$ and $R_{p,m}$.

significant drop in OCV in 200 h of exposure. The OCV was also constant in the test on the LSM 80-98 between 19 and 187 h (Fig. 21, right, pink band) under lab air. However, the thermodynamics of hydrogen oxidation dictates that OCV in air will be higher at 900 °C than at 1,000 °C, regardless of LSM composition: 1.11 V (pink band) vs. 1.01 V. For the rest of the LSM 80-98 test, with p_{O_2} = 0.10, thermodynamics reduces OCV to 1.07 V. Toggling between air and low oxygen at 19 and 187 h showed these changes, which have nothing to do with cell degradation. However, continuous exposure to low p_{O_2} from 187 to the end of the test at 500 h led OCV to drop to 1.04 V, for a degradation rate of 9% per kh. While that is low compared to the degradation rates during durability testing in this work, it is high considering that the cell is doing no electrochemical work. It establishes a baseline degradation rate, attributable to temperature and atmosphere alone, of 9% per kh for performance degradation at p_{O_2} = 0.10 and 900 °C.

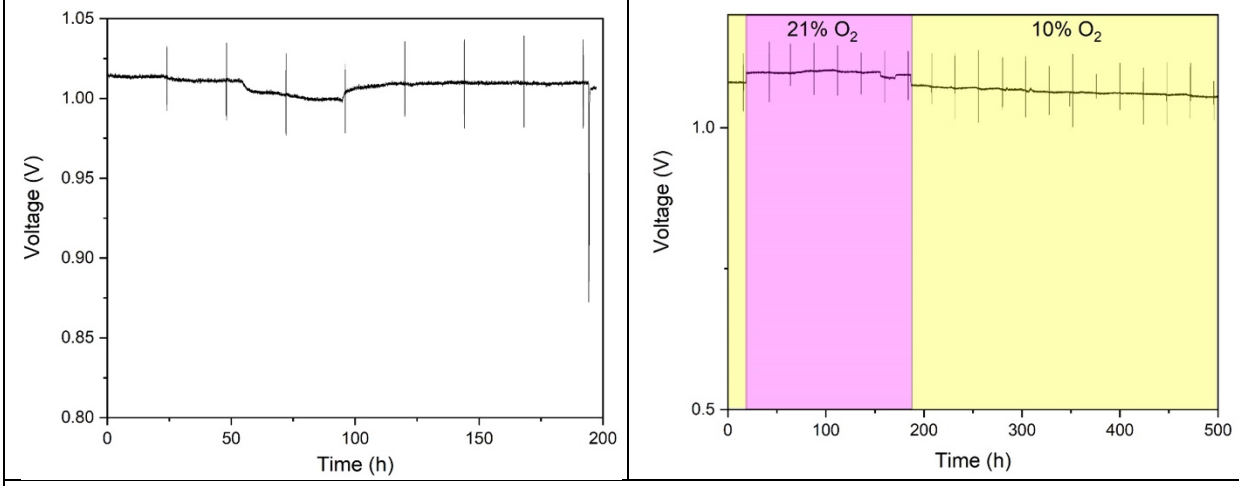

Figure 21. Aging tests (OCV vs. time). Left: cell with LSM 85-90 cathode, 1,000 °C, air, 209 h. Right: LSM 80-98, 900 °C, 10% O_2 (balance N_2) except hours 19 to 187, when the cathode atmosphere was air; 500 h total.

LSV measurements (Figure 22), as the only part of aging tests that place an electrochemical load on the cell (for a few minutes per sweep), give evidence that cell performance was degrading during these tests. Power density, and the current density at which power was (or would have been) maximum, dropped steadily with aging time in both cells. Expected differences due to operating temperature are evident: at equivalent current densities and times, the cell at 1,000 °C gave higher power than the cell at 900 °C. In the 500-h test (Fig. 22, right) note that the LSV sweep in air at 88 h, when the cathode atmosphere was air, gave higher voltage and power than all of the other sweeps, which were under cathode p_{O_2} of 0.10.

Nyquist plots (Fig. 23; fitting results in Table 4) give additional evidence of cell degradation during these aging tests. In the test in air (Fig. 23, left; Table 4, top), all components of ASR_{EIS} increased (shifted to the right) with aging time. At that test's temperature of 1,000 °C, all components of ASR were expected to be, and were, lower than for the test at 900 °C (notwithstanding the differences in LSM composition).

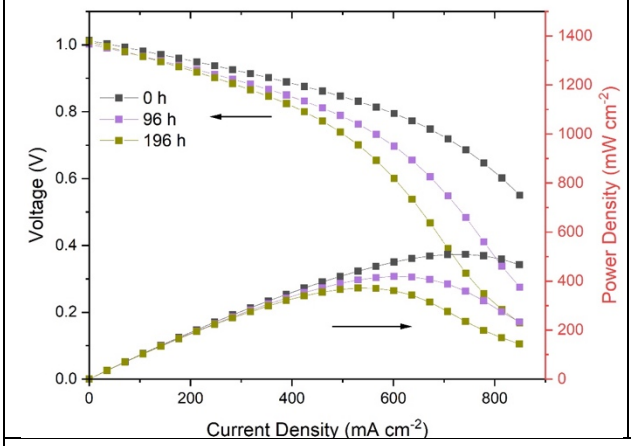

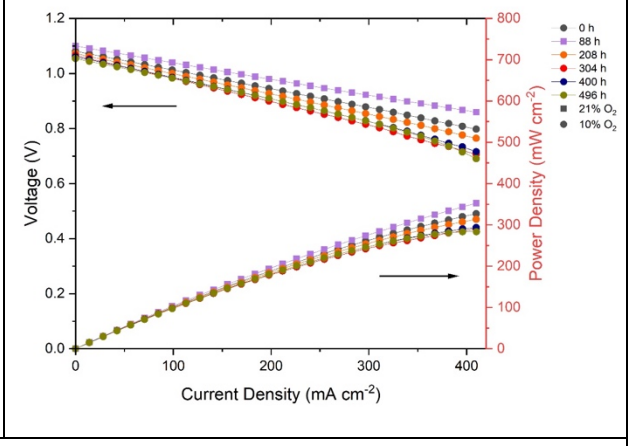

Figure 22. Selected LSV measurements every ~100 h during the aging tests of Figure 21. Left: cell with LSM 85-90 cathode, 1,000 °C, air. Right: LSM 80-98, 900 °C, 10% O_2 (balance N_2) except hours 19 to 187, when the cathode atmosphere was air.

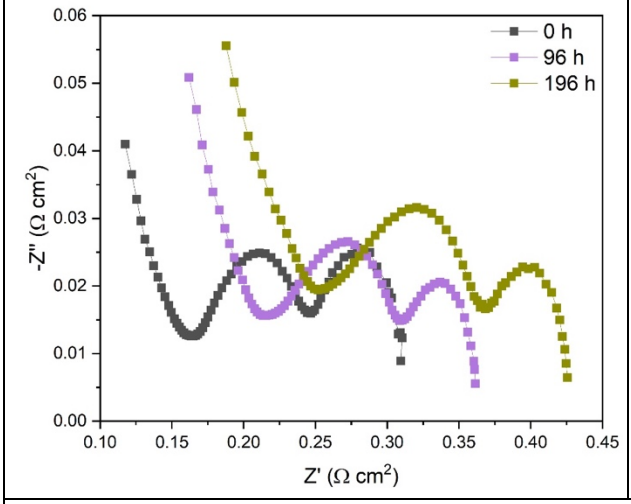

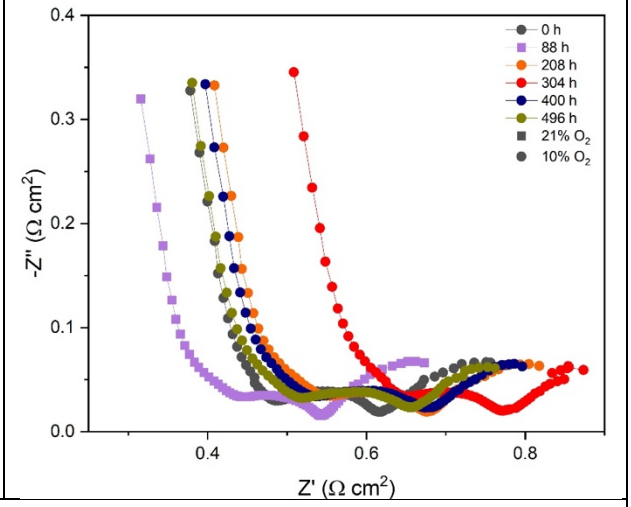

Figure 23. Selected Nyquist plots every ~100 h during the aging tests of Figure 21. Left: cell with LSM 85-90 cathode, 1,000 °C, air. Right: LSM 80-98, 900 °C, 10% O_2 (balance N_2) except hours 19 to 187, when the cathode atmosphere was air.

The trends of ASR_{EIS} and its components in the 900 °C test (Fig. 23, right; Table 4, bottom) are more complex. First, the EIS reading at 88 h was during the period when the cathode atmosphere was air; the impedance and the components of ASR all decreased relative to the preceding readings at low oxygen, as expected. Apart from that, at p_{O_2} = 0.10 the trends were still not monotonic with time: they rose from 0 to 208 to 304 h, then dropped markedly at 400 and slightly at 496 h, but was still above the ASR at 0 h when the test was ended. An explanation for the temporary decreases in ASR between 304 and 496 h is not evident. (Figure 22 right shows similar rises and falls, but they are harder to see because of overlap of the curves.) Table 4 shows the fitting results of Fig. 23. For the test in 10% oxygen, the rise in ASR_{EIS} in the first 304 h was 78.3% per kh, decreasing to 14.6% per kh after 496 h. Again, these effects are due just to exposure of the cell over time at 900 °C under 10% oxygen, with no electrochemical work done.

	t, h	$R_{s,h}$, Ω cm^2	$R_{p,h}$, Ω cm^2	$R_{s,m}$, Ω cm^2	$R_{p,m}$, Ω cm^2	ASR_{EIS}, Ω cm^2
LSM 85-90, aging test at 1,000 °C, air, 209 h.	0	—	—	0.162	0.097	0.259
	96	—	—	0.219	0.100	0.320
	192	—	—	0.264	0.111	0.375
	t, h	$R_{s,h}$, Ω cm^2	$R_{p,h}$, Ω cm^2	$R_{s,m}$, Ω cm^2	$R_{p,m}$, Ω cm^2	ASR_{EIS}, Ω cm^2
LSM 80-98, aging test at 900 °C, 10% O_2 (balance N_2) except hours 19 to 187 in air, 500 h total.	0	—	—	0.455	0.179	0.634
	88 (air)	—	—	0.392	0.169	0.561
	208	—	—	0.514	0.182	0.696
	304	—	—	0.627	0.158	0.785
	400	—	—	0.524	0.165	0.689
	496	—	—	0.496	0.184	0.680

Table 4. Results for equivalent circuit fitting during aging tests. All runs were fit with one semi-circle. Top: a cell with an LSM 85-90 cathode, aged at 1,000 °C, air, 209 h. Bottom: a cell with an LSM 80-98 cathode, aged at 900 °C, 10% O_2 except hours 19 to 187 in air, 500 h total.

Figure 24 shows the microstructure of the LSM 80-98 cathode after the 500-h aging test at 900 °C and p_{O_2} = 0.10. No MnO_x particles are unambiguously present. (Given the limitations of SEM/EDS mapping discussed above, the presence of MnO_x particles about 0.2 μm or smaller cannot be ruled out.)

The finer scale of the microstructural features in this cathode (Fig. 24), and the absence of densification at the cathode/electrolyte interface, even after 500 h of aging at 900 °C in low oxygen cathode atmosphere, are noticeable compared to the LSM 85-90 cathode (Fig. 16).

Figure 25 shows the thresholding of a different BSE image at the cathode-electrolyte interface of this cell: pores (33.4±4.2)%; LSM (39.7±3.8%); YSZ 26.9%. Compared to an as-received LSM 80-98 cathode analyzed using 3DR in the prior project — pores (28±3)%, LSM (35±3)%, YSZ (37±3)% — the LSM and pore fractions exhibit reasonable agreement, whereas the YSZ fraction is low (even considering that the uncertainty in the YSZ fraction is the sum of the uncertainties in the pore and LSM fractions).

In higher-resolution TEM/EDS analysis of LSM 80-98 cathodes in the prior project, in the as-received state (not shown here), after testing at 900 °C and 0.38 A cm^{-2} in air for 500 h (Fig. 26, top) and at 1,000 °C at 0.76 A cm^{-2} for 500 h (Fig. 26, bottom), no MnO_x particles were ever detected.

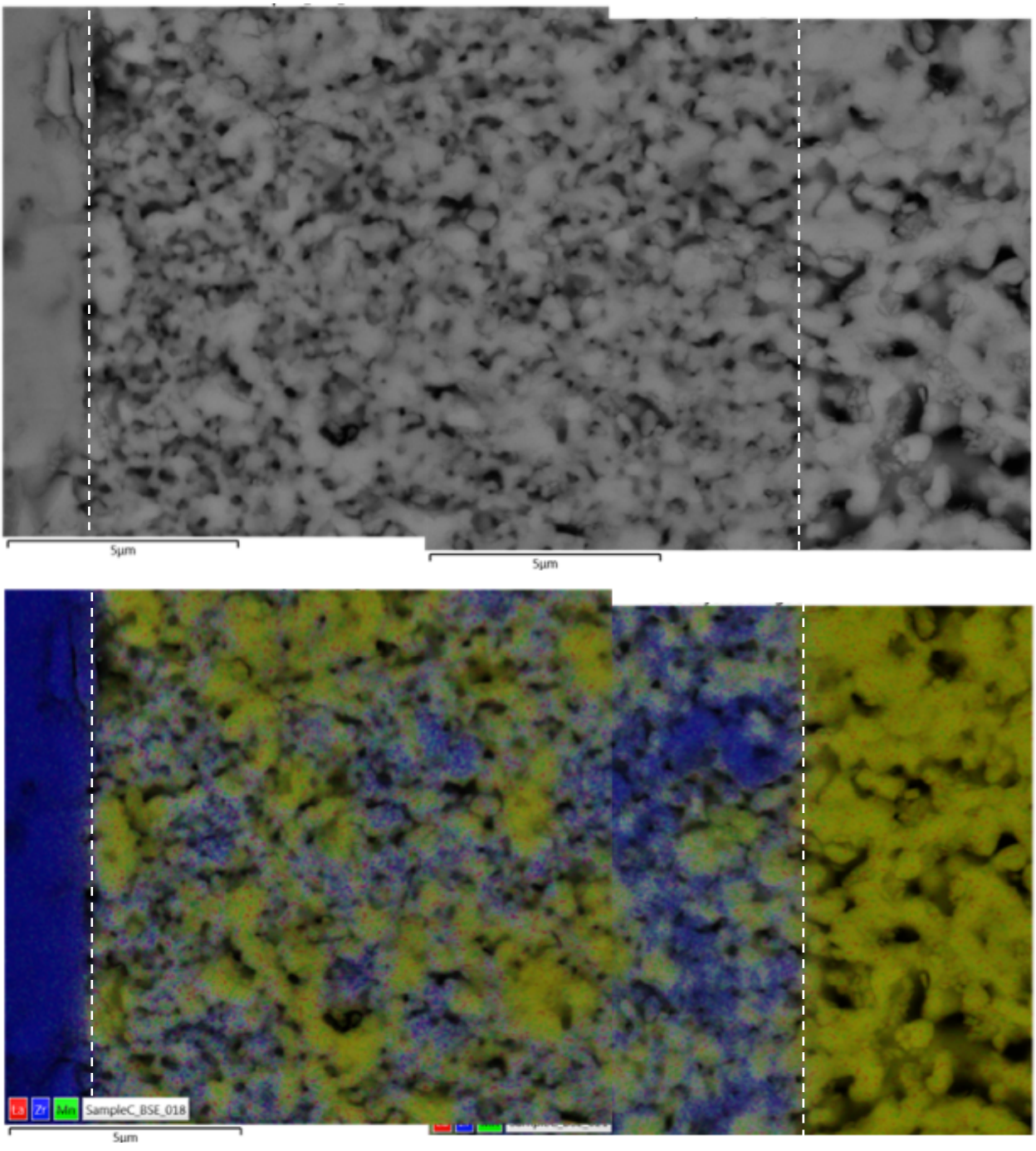

Figure 24. Spliced images of an LSM 80-98 cathode, after testing at 900 °C at OCV in p_{O_2} = 0.10 *for 500 h. From left to right: electrolyte, cathode, cathode current collector (CCC). Top: BSE images. Bottom: EDXS maps (La, Zr, Mn). YSZ appears blue; LSM, yellow or yellow-orange; pores, black. No* MnO_x *particles are evident.*

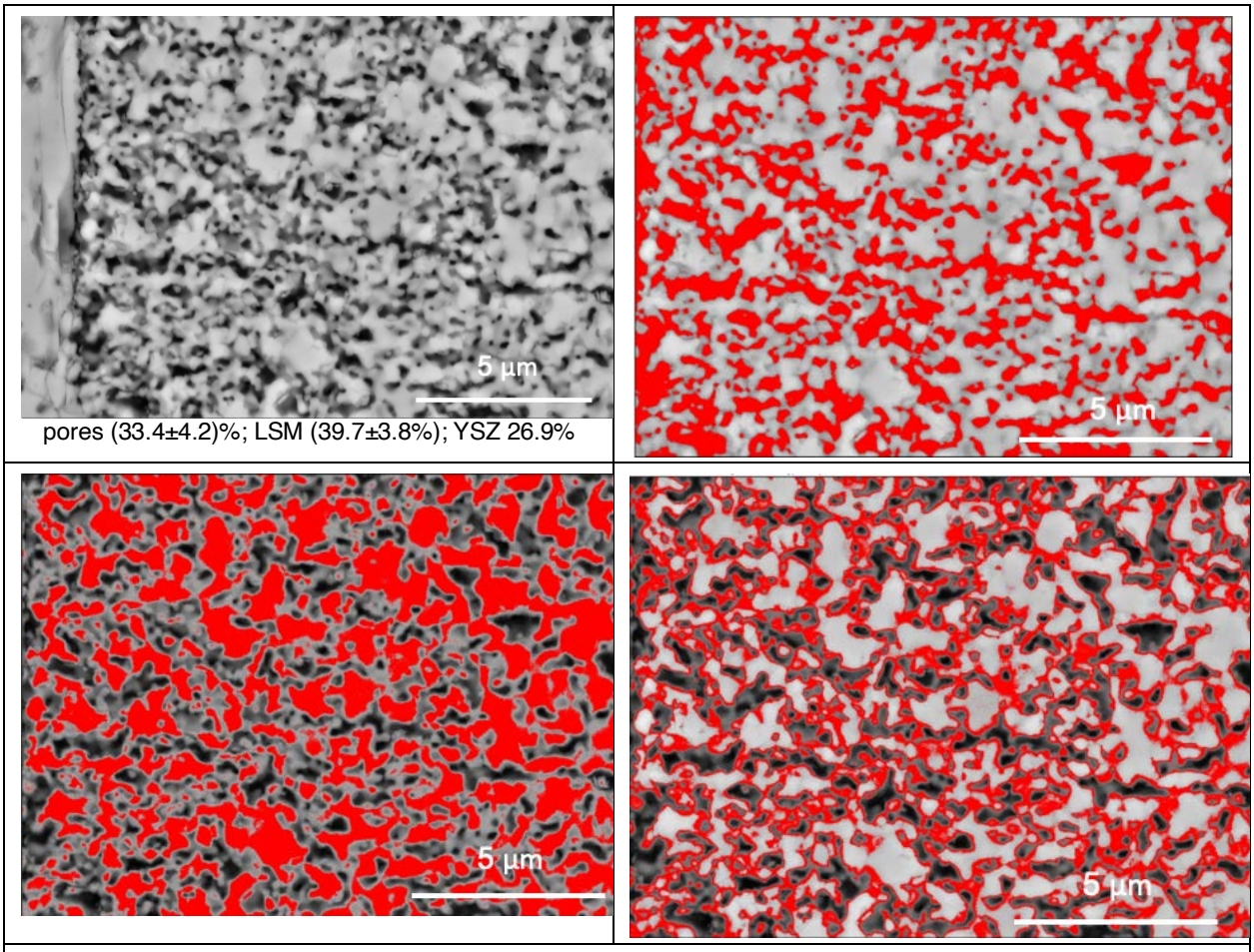

Figure 25. Estimation of phase fractions of the cathode-electrolyte interface, in the same cell as Figure 24 (but a different region) Upper left: original BSE image; volume fractions equal pixel fractions in the thresholded images. Upper right: pores in red (gray level 0–132). Lower left: LSM in red (173–255). Lower right: YSZ in red (133–172).

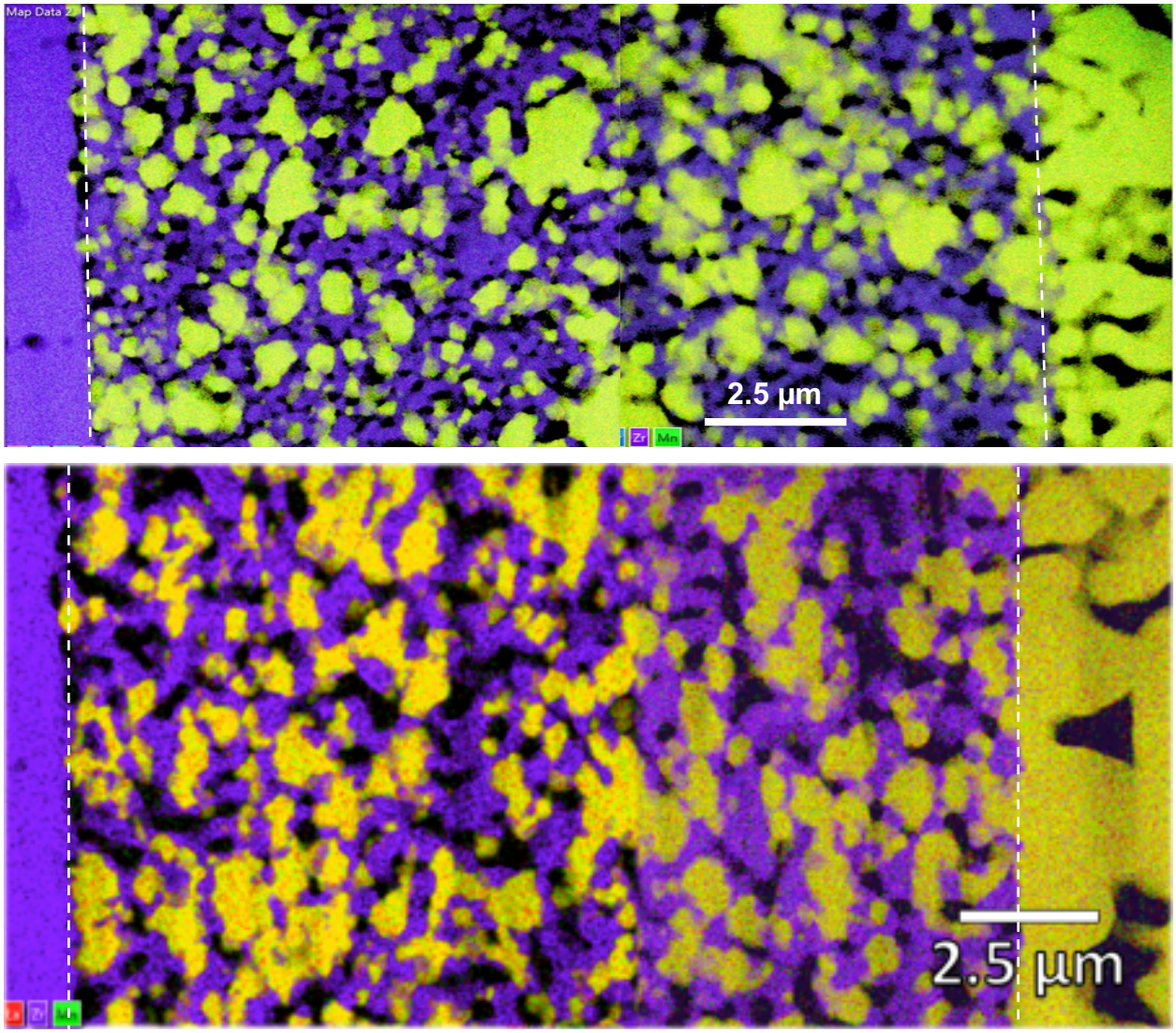

Figure 26. TEM image with superimposed EDS mapping of LSM 80-98 cathodes after durability testing for 500 h in air from the previous project [31]. Top: at 900 °C, 0.38 A cm^{-2}. Bottom: at 1,000 °C, 0. 76 A cm $^{-2}$.

Unlike the LSM 85-90 cathode (Figs. 16, 17) with 11% excess Mn, LSM 80-98 has just 2% Mn excess. Clearly, prior work showed that low Mn excess discourages the appearance of MnO_x in LSM cathodes under extended testing in air, even at temperature and high current density after 500 h. The present work adds aging at 900 °C and p_{O_2} = 0.10 to the list of conditions that are insufficient to lead to MnO_x formation in LSM 80-98 / 8YSZ cathodes. An extended durability test at low p_{O_2} and aggressive conditions remains to be achieved, but such an experiment would be the next logical test of the stability of LSM 80-98 against MnO_x formation.

LSM 80-95, 900 °C, 0.38 A cm^{-2}, 10% O_2, 58 h. This cell was tested under a cathode environment of 10% O_2 (balance N_2) using the titanium test fixture described above. The test ran normally for 58 h, at which point thermal stresses between the fixture and the cell support tube caused the tube to crack, introducing air into the anode atmosphere and leading to abrupt failure of the cell.

Before the start of the durability test, the parametric tests for this cell (Fig. 27, left) showed expected dependences on temperature and cathode atmosphere (cell ASR rising with decreasing temperature and with decreasing-p_{O_2}). Results of equivalent-circuit fits to the parametric tests (Table 3) support these trends for all circuit components and temperatures in most cases.

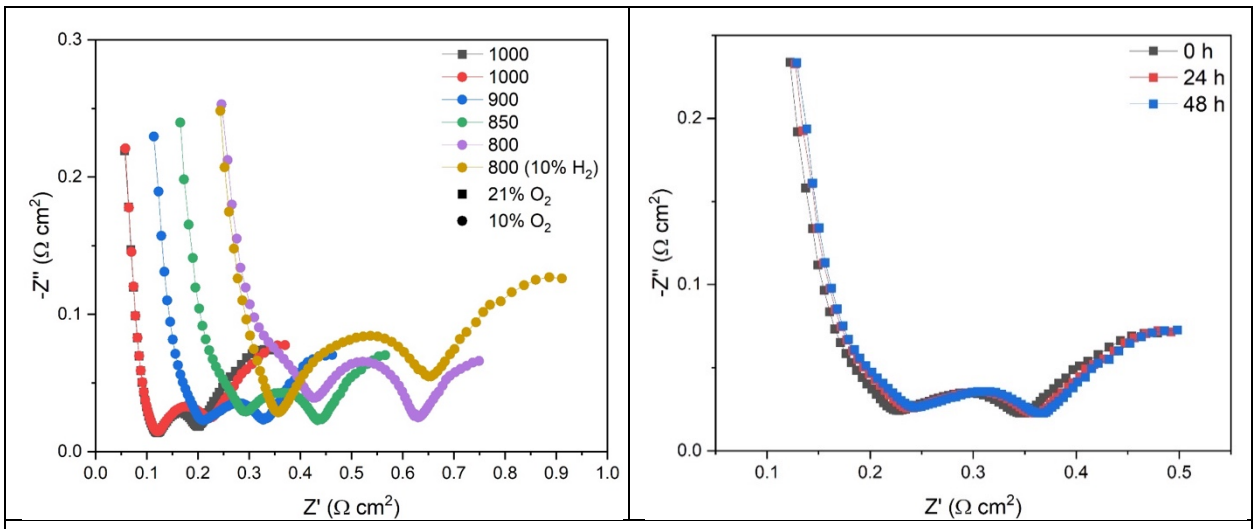

Figure 27. Nyquist plots from a cell with an LSM 80-95 cathode, tested at 900 °C, p_{O_2} = 0.10, 0.38 A cm^{-2}, 58 h. Left: Parametric testing at t=0. Right: During durability test at 0, 24, 48 h.

Figure 28, left shows the cell output voltage and electrode ASR_{DC} from this test. Cell output was stable but dropped sharply when the cell support tube cracked at 58 h. Electrode ASR_{DC} rose from 0.263 to 0.276 Ω cm^2 in 58 h (85% per kh); total cell ASR rose 65% (Fig. 35). Figure 28, right shows LSV sweeps at 0, 24, and 48 h from this test. In that representation, the change with time is so slight that the three V-I curves essentially overlap, as do the three P-V curves. The ASR_{LSV} from this plot is 0.43 Ω cm^2, which gives an $ASR_{e'ode}$ of 0.21 Ω cm^2 per eq. 7 and Table 1, in approximate agreement with the values of electrode ASR_{DC} in Figure 28, left.

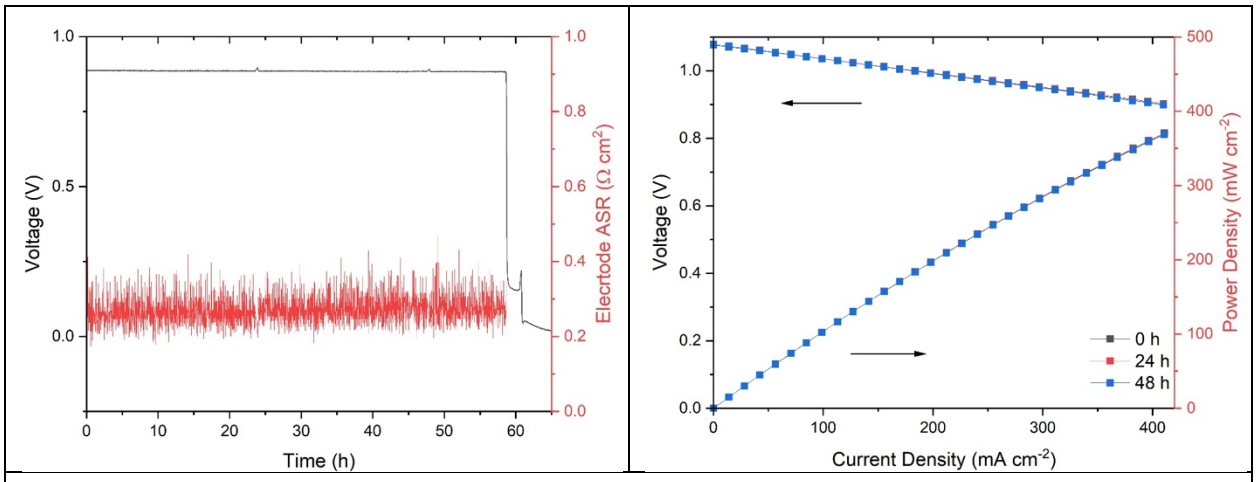

Figure 28. Durability test of a cell with an LSM 80-95 cathode, 900 °C, p_{O_2} = 0.10, 0.38 A cm^{-2}, 58 h. Left: Voltage and electrode ASR_{DC} vs. time. Right: LSV sweeps at 0, 24, 48 h.

Because of the stable cell output in the short test before the fixture failed, the Nyquist plots from parametric tests and EIS measurements taken in the first 58 h of this test should give a clear picture of normal cell operation at 900 °C in p_{O_2} = 0.10 cathode atmosphere and 0.38 A cm^{-2}. Figure 27, left shows the normal progression of parametric tests, with Z' and Z'' increasing with decreasing temperature from 1,000 °C to 800 °C. At 1,000 °C, the leftmost minimum (roughly, R_s) was unaffected by the change from air (black squares) to 10% oxygen (red circles), whereas the rightmost minimum increased in both Z' and Z'' on the shift to low p_{O_2}, suggesting increases in R_p components such as electrode (possibly cathode) processes. Quantitative results of equivalent-circuit fits to the parametric tests (Table 5) generally support these qualitative trends. As the durability test proceeded (Fig. 27, right), ASR_{EIS} increased steadily but slightly with time, equal to 67.2% per kh (Table 5), in excellent agreement with the value of 65.1% per kh in cell ASR_{DC} (Fig. 35).

Test	T, °C	$R_{s,h}$[10], Ω cm^2	$R_{p,h}$, Ω cm^2	$R_{s,m}$, Ω cm^2	$R_{p,m}$, Ω cm^2	ASR_{EIS}, Ω cm^2
LSM 80-95, 10% O_2, t=0 (before durability testing)	1,000 (air)	—	—	0.117	0.094	0.211
	1,000	—	—	0.114	0.129	0.243
	900	—	—	0.206	0.143	0.348
	850	—	—	0.264	0.194	0.458
	800	0.235	0.209	0.410	0.231	0.641
	800 (10% H_2)	—	—	0.396	0.291	0.687
LSM 80-95, durability testing at 900 °C, 10% O_2, 0.38 A cm^{-2}.	t, h	$R_{s,h}$, Ω cm^2	$R_{p,h}$, Ω cm^2	$R_{s,m}$, Ω cm^2	$R_{p,m}$, Ω cm^2	ASR_{EIS}, Ω cm^2
	0	—	—	0.208	0.163	0.372
	24	—	—	0.217	0.167	0.384
	48	—	—	0.229	0.155	0.384

Table 5. Results for equivalent circuit fitting of a cell with an LSM 80-95 cathode, tested at 900 °C, p_{O_2} = 0.10, 0.38 A cm^{-2}, 58 h. Runs for which no values are given for $R_{s,h}$ and $R_{p,h}$ were fit with a single semicircle; otherwise the fits used two semicircles.

Figure 29 shows side-by-side BSE (left) and SEM/EDS (right) images of the entire width of this LSM 80-95 cathode after testing. In this cell, many more assignments could be made of possible small (100–200 nm) MnO_x grains through the cathode, on the basis of medium-gray grains that coincided with high EDS Mn signals. This contrasts with the smaller number, larger size, and location of MnO_x particles near the cathode/electrolyte interface in the LSM 85-90 cell tested for 1,008 h in air (Fig. 16). In the other direction, the aged LSM 80-98 cell (Fig. 24) showed fewer suspected MnO_x grains, but they are small and evenly distributed across both of those cathodes. Their greater number in LSM 80-95 is compatible with the higher Mn excess (5% vs. 2%) in LSM 80-95 vs LSM 80-98.

[10] Due to the limitation of NOVA software, only one arc can be fit at a time. Hence, the $R_{s,h}$ is treated as the R_s of the cell and ASR is the sum of $R_{s,m}$ and $R_{p,m}$.

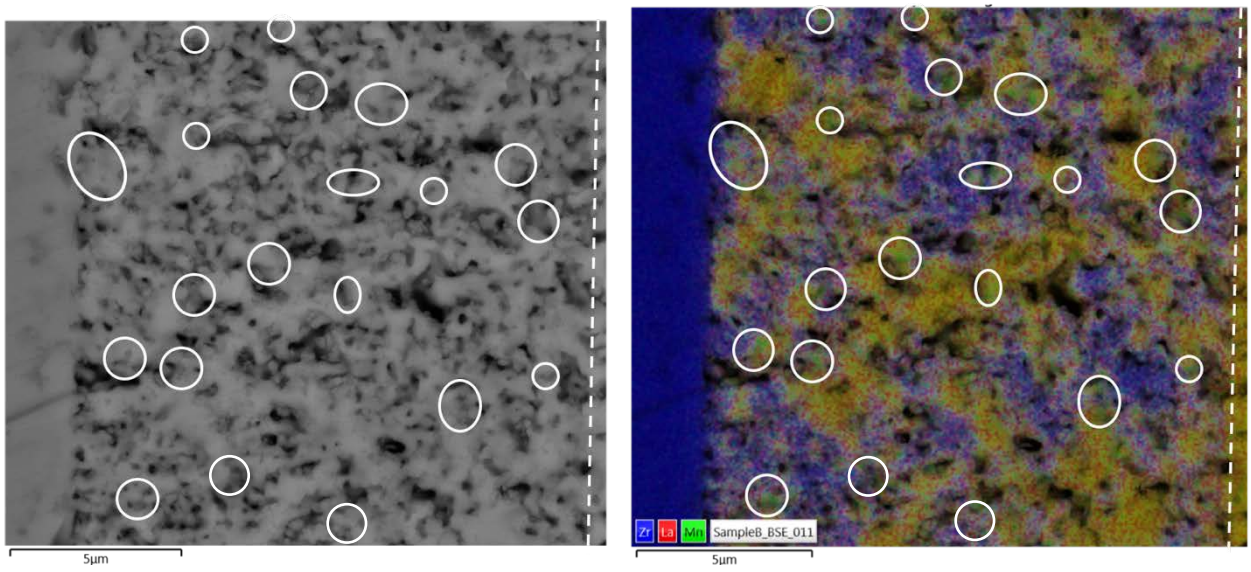

Figure 29. SEM images of the LSM 80-95 cathode tested under 10% O_2 (balance N_2), 900 °C, 0.380 A cm^{-2} for 58 h. Left: BSE; right: SEM/EDS. The electrolyte is at the left edge, and the cathode/CCC interface is at the right edge (white dashed line) of each image. In the right image, YSZ appears blue, LSM yellow, and pores black. White circles indicate tentative identifications of MnO_x: medium-grey grains (left) that coincide with high Mn EDS signals (green, left).

Figure 30 shows the thresholding of the cathode in Figure 29: pores (36.1±4.8)%; LSM (33.6±6.1)%; YSZ 30.3%. Compared to an as-received LSM 80-95 cathode analyzed using 3DR in the prior project — pores (29±3)%, LSM (38±3)%, YSZ (33±3)% — all phase fractions agree within the uncertainties, the LSM and YSZ better than the pore fraction.

In the prior project, MnO_x particles were occasionally observed in LSM 80-95 cathodes and CCC, as received and after durability testing in air (Fig. 31). Figure 29 therefore gives tentative support to the possibility that durability testing in low-p_{O_2} cathode atmosphere (even a relatively short test of <70 h) increases the likelihood of MnO_x formation.

Table 6 summarizes the phase fraction results for 10 BSE images across three of the cells that were discussed in depth in this section. In general, both the uncertainty of LSM and YSZ fractions, and the spread of LSM and YSZ fractions from image to image, were sometimes large. Still the averages of the phase fractions over multiple images of the same cathode were usually in good agreement with the results from 3DR of the as-received cathodes. In any event, the uncertainties in Table D are larger than any changes that might be attributed to microstructure change during testing.

Another advantage of 3DR (carried out in the previous project, but not here) is that the average fractions for each phase come from 90–150 separate images. The statistical standard deviation over all of those images was smaller than the ±3% given in the table; ±3% represents reproducibility between repeated 3DR analyses of different but nominally identical specimens. 3DR also enables phase fraction profiles to be determined reliably across a cathode; the small number of separate images analyzed in this work would not give reliable quantitative profiles.

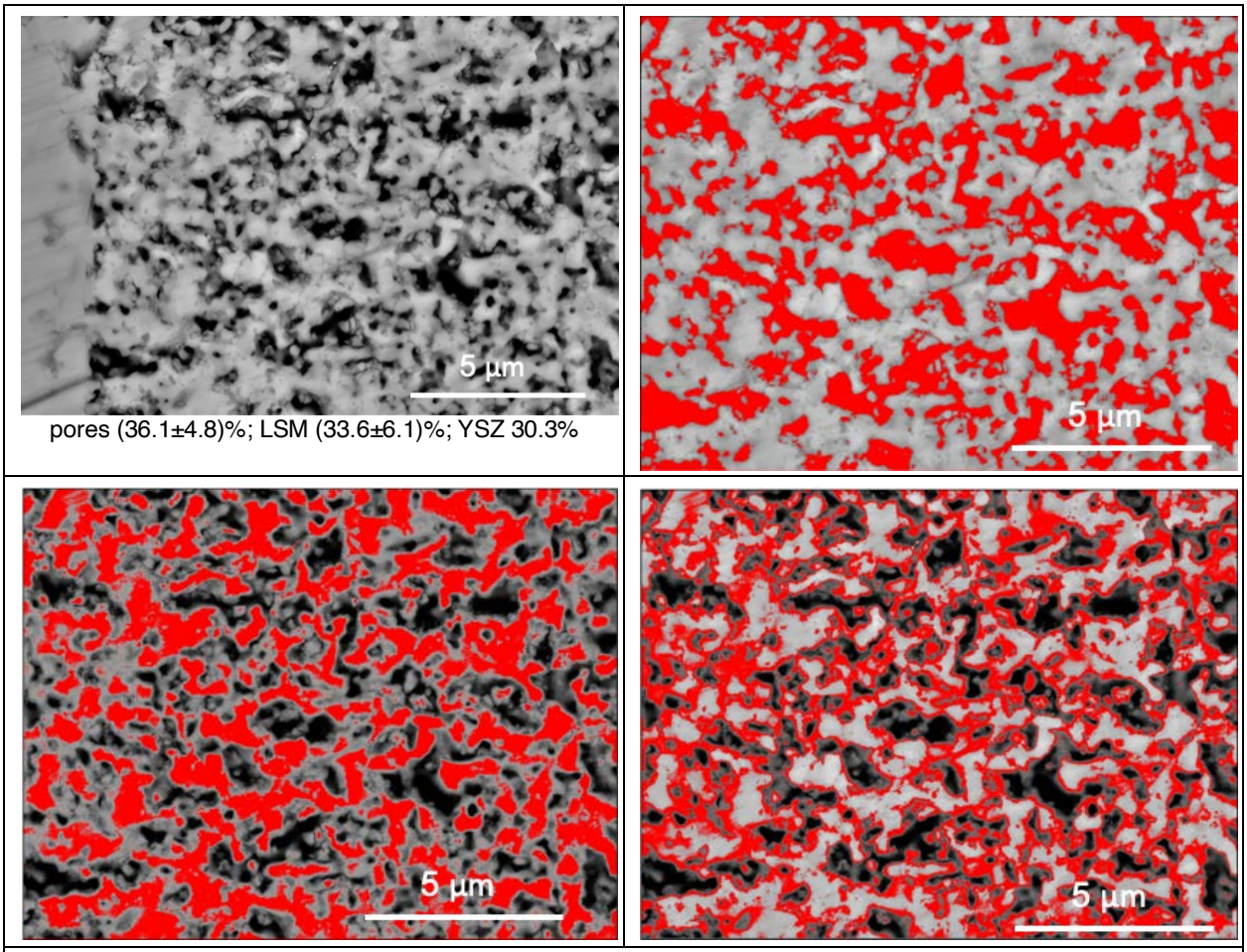

Figure 30. Estimation of phase fractions across the cathode of Figure 29. Upper left: BSE image; volume fractions equal pixel fractions in the thresholded images. Upper right: pores in red (gray level 0–123). Lower left: LSM in red (166–255). Lower right: YSZ in red (124–165).

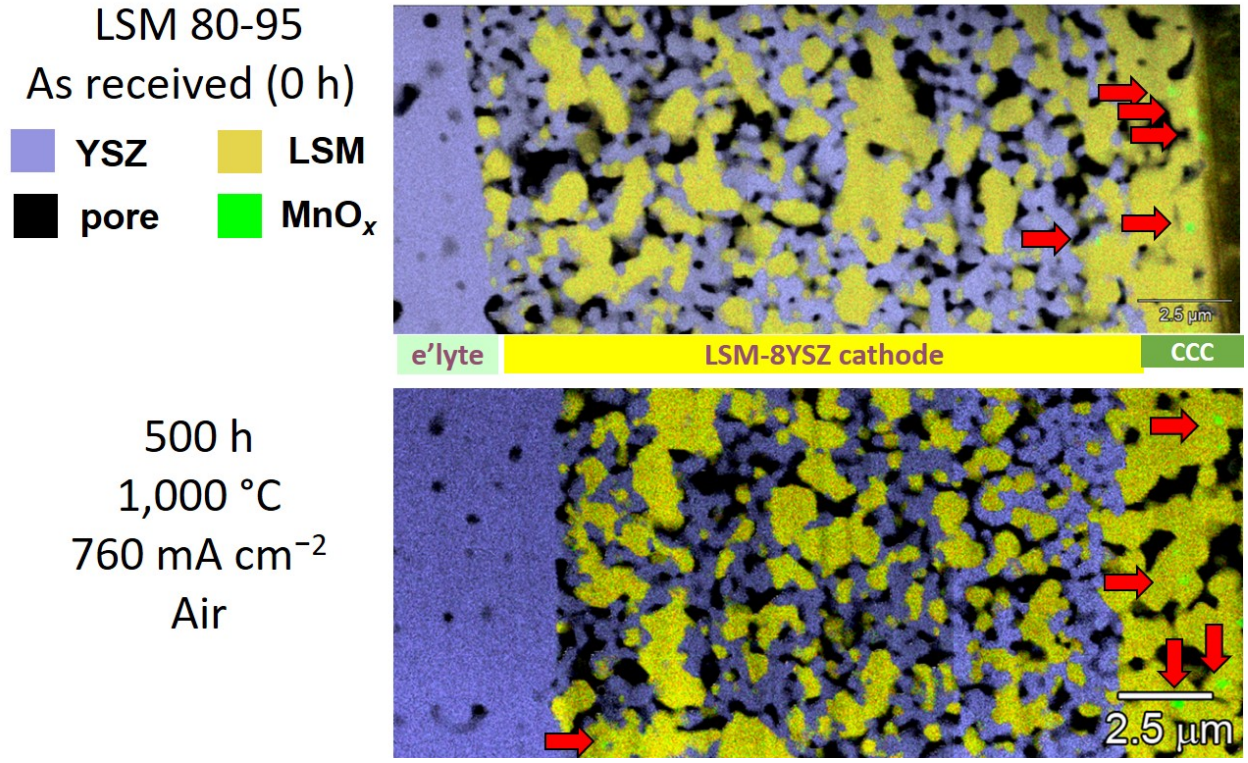

Figure 31. TEM images of LSM 85-90 cathodes with superimposed EDS maps. Top: as received. Bottom: after testing in air at 1,000 °C, 760 mA cm $^{-2}$ for 500 h. From previous study [31].

LSM 85-90, 1,000 °C, air, 0.76 A cm^{-2}, 1,008 h	pores, vol%	LSM, vol%	YSZ, vol%
C/CCC, 10k×,a	26±4	46±11	28
C/CCC, 10k×,b	22±3	29±12	49
C/E, 10k×,a	21±3	35±14	44
C/E, 10k×,b	25±4	42±6	33
C/E, 7.5 k×	27±4	42±6	31
C/E/CCC, 7.5 k×	24±4	41±6.3	35
average	24.1±3.2	39.2±10.1	36.6±12.5
as received (3DR)	23±3	41±3	35±3
LSM 80-98, 900 °C, 10% O_2, aging, 500 h	33±4	40±4	27
as received (3DR)	28±3	35±3	37±3
LSM 80-95, 10% O_2, 900 °C, 0.38 A cm^{-2}, 58 h			
C/E, 10k×	34±6	37±5	30
C/CCC, 10k×	38±5	27±6	35
C/E, 7.5k×	36±5	34±6	30
C/E, 10k×	30±5	31±5	39
average	34.4±4.2	32.1±4.8	33.5±5.5
as received (3DR)	29±3	38±3	33±3

Table 6. Summary of phase fraction determinations in cathodes from three tested cells.

LSM 80-95, 1,000 °C, 0.76 A cm^{-2}, air, 303 h. In contrast to the preceding example on a cell with an LSM 80-95 cathode, this cell was tested with air as the cathode environment at 1,000 °C and current density of 760 mA cm^{-2}. The cell exhibited a strong voltage drop at ~60 h (Fig. 32, left), and the test was first ended at 68 h. The cell was cooled to room temperature (20 ℃) at 3 ℃/min, held for 143 h, then heated back to 1,000 ℃ at the same rate. The test proceeded until a Windows update interrupted the test, for a total time of 303 h under load. Post-test examination indicated that the lab-made type-K thermocouple was heavily oxidized during the test, which might have caused the furnace temperature to be lower than 1,000 ℃, resulting in the abnormally decreased voltage readings after 215 h (Fig. 32, left).

Figure 33 left shows the normal progression towards increasing impedance with decreasing temperature for a test in air as the cathode atmosphere. Figure 33 right shows that the cell resistance increased slightly but steadily with time until the suspected thermocouple problems occurred after 200 h. The results of equivalent-circuit fits (Table 7) to these Nyquist plots supports these trends.

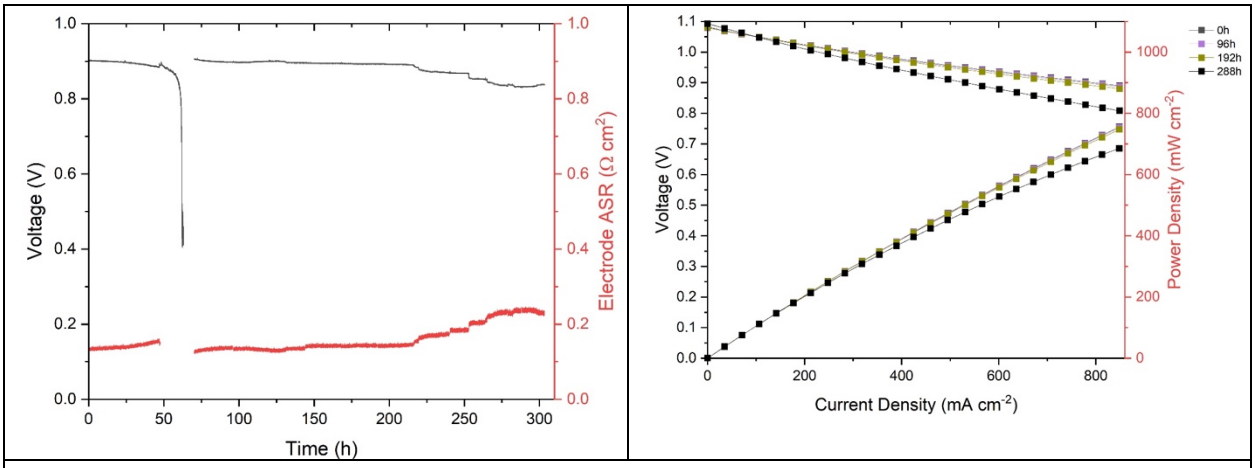

Figure 32. Test of a cell with an LSM 80-95 cathode at 1,000 °C and 0.38 A cm^{-2} in air for 303 h. Left: Cell voltage and electrode ASR_{DC} vs. time. Right: LSV sweeps every ~100 h.

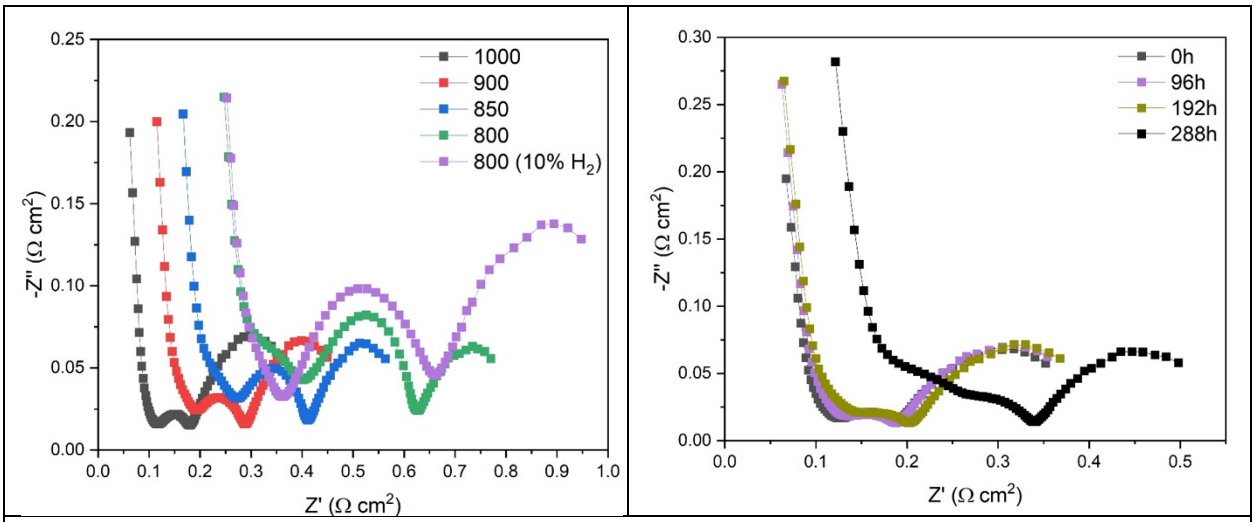

Figure 33. Nyquist plots from a cell with an LSM 80-95 cathode, tested at 1,000 °C in air, 0.76 A cm^{-2}, 303 h. Left: Parametric testing at t=0. Right: During durability test, every ~100 h.

Test	T, °C	$R_{s,h}$[11], Ω cm^2	$R_{p,h}$, Ω cm^2	$R_{s,m}$, Ω cm^2	$R_{p,m}$, Ω cm^2	ASR_{EIS}, Ω cm^2
LSM 80-95, air, t=0 (before durability testing)	1,000	—	—	0.113	0.088	0.202
	900	—	—	0.171	0.130	0.301
	850	0.118	0.170	0.271	0.146	0.416
	800	0.126	0.324	0.423	0.204	0.626
	800 (10% H_2)	0.127	0.250	0.363	0.312	0.675
LSM 80-95, durability testing at 1,000 °C, air, 0.76 A cm^{-2}.	t, h	$R_{s,h}$, Ω cm^2	$R_{p,h}$, Ω cm^2	$R_{s,m}$, Ω cm^2	$R_{p,m}$, Ω cm^2	ASR_{EIS}, Ω cm^2
	0	—	—	0.113	0.088	0.202
	96	—	—	0.111	0.094	0.205
	192	—	—	0.117	0.103	0.220
	288	—	—	0.204	0.148	0.352

Table 7. Results for equivalent circuit fitting of a cell with an LSM 80-95 cathode, tested at 1,000 °C, air, 0.76 A cm^{-2}, 303 h. Runs for which no values are given for $R_{s,h}$ and $R_{p,h}$ were fit with a single semicircle; all others were fit with two semicircles.

Figure 34 puts the results of the initial parametric tests on LSM 80-95 cathodes in low oxygen (Fig. 27 left) side-by-side with those in air (Fig. 33, left). Both cells gave nearly identical readings at 1,000 °C in air (black squares). When the cathode atmosphere was p_{O_2} = 0.10, the LSM

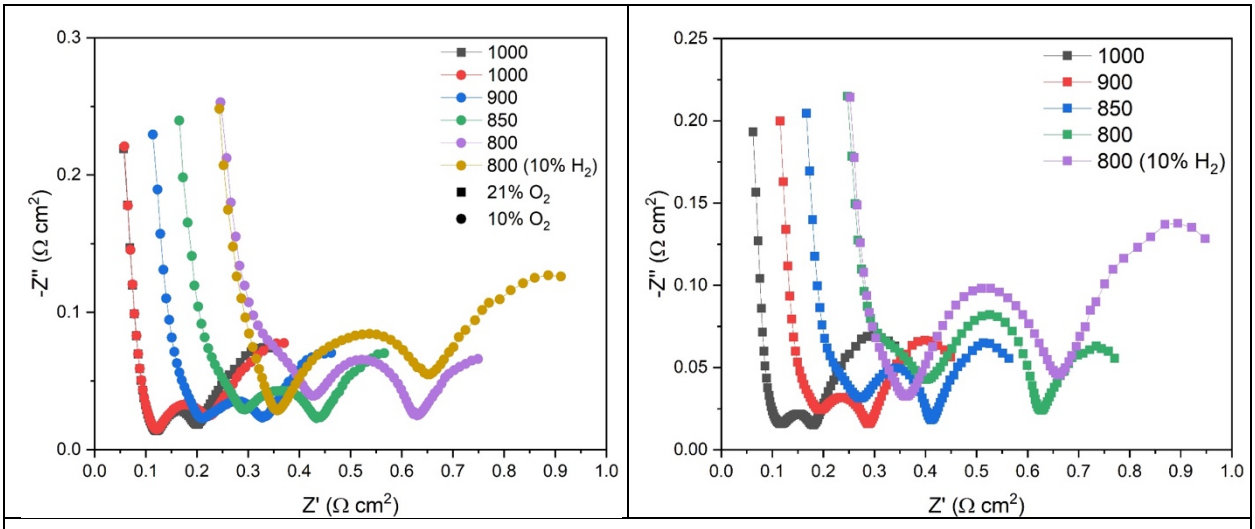

Figure 34. Nyquist plots from cells with LSM 80-95 cathodes prior to durability testing: under cathode atmospheres of p_{O_2} = 0.10 (left) and air (right).

[11] Due to the limitation of NOVA software, only one arc can be fit at a time. Hence, the $R_{s,h}$ is treated as the R_s of the cell and ASR is the sum of $R_{s,m}$ and $R_{p,m}$.

80-95 cathode exhibited consistently 5–10% higher impedance than in air at equivalent temperatures. That shows that low oxygen on the cathode side results in an almost immediate increase in cell ASR, independent of any long-term degradation effects of low oxygen exposure.

ASR from durability testing, EIS, and LSV measurements. As discussed in the Approaches used section, the change of cell ASR during its operating lifetime can be computed three different ways from the data collected in this work (Eqs. 4–6):

- ASR_{DC}, from the variation in continuous cell output voltage versus time during durability tests. By subtracting electrolyte ASR (assumed to be constant during testing, Table 1) from total cell ASR_{DC}, an electrode ASR_{DC} can be computed (e.g. Figs. 15, 28, 32)
- ASR_{EIS}, from fitting equivalent circuit models to the daily EIS measurements during aging or durability tests (e.g. Figs. 9, 10, 14; Tables 2–7)
- ASR_{LSV}, from slopes of linear ranges of *V–I* curves obtained in daily LSV measurements during aging or durability tests (e.g. Fig. 11).

Each approach is an independent measurement of cell ASR, and can be expected to give similar but not identical values. In all three cases, the temperature and atmosphere are the same as those of the contemporaneous durability or aging test. ASR_{DC} reflects cell DC output at constant current load, but cannot be measured during aging tests. ASR_{EIS} comes from modeling impedance spectra obtained at very low AC current systematically stepped from 100 kHz to 0.01 Hz. Like ASR_{DC}, ASR_{LSV} comes from DC measurements, but while current density is systematically stepped from zero to 0.85 A cm^{-2} (0.40 A cm^{-2} when the durability or aging test is at 900 °C).

Figure 35 presents all three versions of ASR as a function of time for four different cells, having three of the four cathode compositions studied in this work. The test shown in the upper left is the 1,008-hour test whose results appear in Figures 13–16 and Table 2. The test shown in the upper right is the one whose results appear in Figures 32–33 and Table 7. The test shown in the lower left is the one whose results appear in Figures 27–30 and Table 5. The test shown in the lower right was on a cell with a composition-D cathode.

In all four tests shown in Figure 35, values of ASR_{DC} were higher than those of ASR_{EIS} and ASR_{LSV}, though ASR_{DC} was only slightly higher than ASR_{EIS} for the 1,008-hour test. The relative magnitudes of ASR_{EIS} and ASR_{LSV} varied from test to test. This may be because of factors unique to each tested cell, such as how closely the equivalent circuit model (used to obtain ASR_{EIS}) described the behavior of the particular cell, or the magnitude of the nonlinear activation losses (which are not included when computing ASR_{LSV}). This illustrates that numerical values of area specific resistance may depend significantly on how it is defined and computed in any given study.

Nevertheless, the trends of area specific resistance with time were similar for any of the three ways of computing ASR, even down to short- and long-term variations. This indicates that area specific resistance remains a valid metric for monitoring changes in cell performance over time, even when different ways of computing it give significantly different values. From the definitions used here (eqs. 4–6), ASR_{DC} provides a direct measure of long-term degradation in cell performance under constant-current conditions, including activation, ohmic, and transport losses, without having to interrupt operation to take a *V-I* curve or impedance spectrum. Computing ASR_{LSV} across a current sweep can indicate how a cell would perform under relevant ranges of variable current loads. Lastly, ASR_{EIS} and its constituent series and parallel resistances can give clues about where in a system (electrodes, catalysts, electrolyte, gas transport processes from the

inlet to the outlet of a stack) degradation might be occurring.

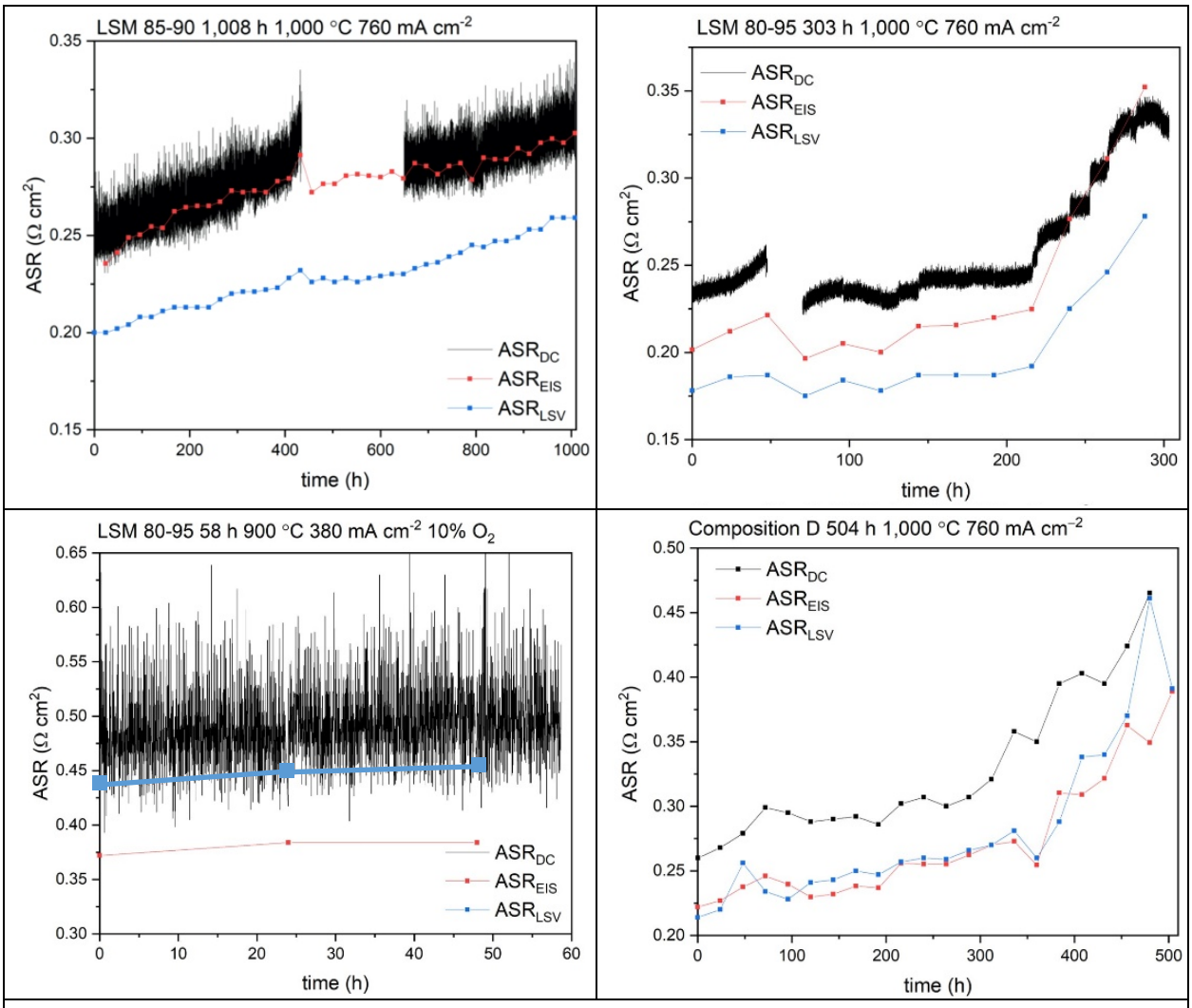

Figure 35. Comparisons of cell ASR versus time measured three ways (eqs. 4–6) during durability tests of four cells under the indicated conditions. Upper left: LSM 85-90 cathode, 1,000 °C, 0.76 A cm^{-2}, air. Upper right: LSM 80-95 cathode, 1,000 °C, 0.76 A cm^{-2}, air. Lower left: LSM 80-95 cathode, 900 °C, 0.38 A cm^{-2}, 10% oxygen. Lower right: Composition D cathode, 1,000 °C, 0.76 A cm^{-2}, air. ASR_{LSV} was computed from the slope of the V-I curves between 0.70 and 0.85 A cm^{-2} for the tests at 1,000 °C, and between 0.35 and 0.40 A cm^{-2} for the test at 900 °C.

DRT analysis: Effect of cathode oxygen content on degradation. DRT analysis reveals how different frequency ranges of the impedance spectra respond to changes in operating conditions. When those changes affect particular parts of the cell (hydrogen levels at the anode, oxygen levels at the cathode), and when those effects can be monitored over time, insights can be gained into possible degradation mechanisms as they evolve. Table 8 summarizes assignments of frequency ranges to loss mechanisms associated with electrochemical and transport processes in SOFCs in the literature [32–38]. Relationships that have been noted in this work are discussed below.

Peak	Frequency, Hz	Literature	In this work
1	$> 10^5$	Ionic transport in YSZ; transport of O-intermediates	
2	$10^4 – 10^3$	Charge transfer between Ni and YSZ	Charge transfer in Ni/YSZ; H_2 adsorption
3	$10^3 – 10^2$	Dissociative adsorption of O_2; gas diffusion	Cathode atmosphere
4	$10^2 – 10^1$	Diffusion and fuel conversion	Fuel composition
5, 6	$10^{-1} – 10^0$, $10^{-2} – 10^{-1}$	Gas diffusion; surface reaction	Gas composition of cathode and anode environment

Table 8. Frequency ranges for loss mechanisms relevant to SOFCs

Figure 36 shows two different cells with LSM 80-98 cathodes at 1,000 °C at the beginning of testing in reduced levels of oxygen (10%, and 15%) on the cathode side. Two effects are notable:

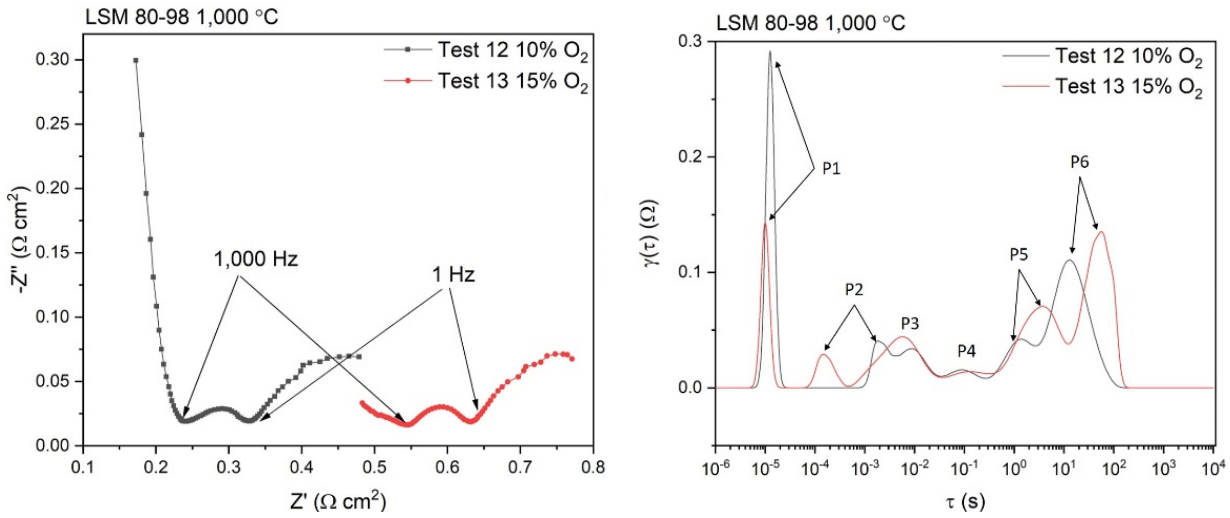

Figure 36. EIS results from two cells with LSM 80-98 cathodes at 1,000 °C and low oxygen content (10% or 15%) on the cathode side before long-term testing. Left: Nyquist plots. Right: DRT analysis.

- For reasons that are unrelated to the cells themselves, the measurement under 10% oxygen exhibited the high-frequency tail (discussed in the Approaches section), but in the measurement under15% oxygen the tail was greatly reduced. This is evident first in the taller high-frequency peak P1 (relaxation time $\tau \cong 10^{-5}$ s) in the test under 10% oxygen. (Lower oxygen content is expected to lead to higher impedance in general, which could also have contributed to the taller P1 in the test under 10% oxygen.) With the reduced high-frequency tail in the test under 15% oxygen, DRT analysis was able to resolve a peak P2 with relaxation time of $\sim 10^{-4}$ s that was obscured by the high-frequency tail in the test under 10% oxygen. In contrast, P2 does not appear until $\tau \cong 2\times10^{-3}$ s in the test under 10% oxygen. It seems unlikely that loss mechanisms at 10^{-4} s and 2×10^{-3} s are unique to operation under 15% and 10% oxygen respectively, especially since these two cathodes were nominally

identical. Since most of the EIS spectra reported here exhibited a high-frequency tail, the absence of peaks at 10^{-4} s in the DRT analyses below should not be interpreted as an absence of loss mechanisms in that range.

- Both spectra show minor loss mechanisms (P3) in the range of 5×10^{-3} s $< \tau <$ 9×10^{-3} s and almost identical small losses centered around 0.1 s (P4). The lowest-frequency peaks, P5 and P6 (1 s $< \tau <$ 100 s) show significant shifts to shorter relaxation times at 10% oxygen (Table 8).
- In general, impedance spectra that exhibited the high-frequency tail had significantly higher χ^2 in the Kramers–Kronig validation test (i.e. more irregular impedance readings). For example, here $\chi^2(Z)$ of the test under 10% was 1.15×10^{-5}, whereas $\chi^2(Z)$ of the test under 15% oxygen was 2.21×10^{-6}.

Figure 37 presents DRT analyses of parametric tests at $t = 0$ for four cells with LSM 80-95 cathodes: two in air (top row), and two in 10% oxygen (bottom row) on the cathode side. Certain observations apply regardless of the cathode atmosphere:

- As temperature decreases:
  - P1 rises. Although the height and position of this peak are dominated by the high-frequency tail artifact in our measurements, the reproducibility of this trend with temperature (seen in all DRT analyses conducted in this work) is consistent with there being a high-frequency ($\tau \cong 10^{-5}$ s) loss mechanism that increases with decreasing temperature. The literature assigns this range to oxygen ion transport in YSZ (Table 8).
  - P2 increases and shifts to shorter values of relaxation time, from $\tau \cong 10^{-3}$ to 2×10^{-3} s.
  - P3 increases, and in some cases shifts to shorter values of relaxation time.
  - P4 rises markedly when the hydrogen level in the anode stream is reduced to 10%, balance nitrogen (from 100% hydrogen). This indicates that P4 is associated at least in part with loss mechanisms at the anode (Table 8).

Some of the features in Figure 37 differ between cathode atmospheres of air (top row) and 10% oxygen (bottom row):

- In air, P2 and P3 overlap at higher temperatures (900 and 1,000 °C) but become more separated as temperature drops (800 and 850 °C).
- In 10% oxygen, P2 and P3 are generally distinct at higher temperatures (900 and 1,000 °C) but P3 begins to overlap with P2, P4, or both as temperature drops (800 and 850 °C).

These observations indicate that the loss mechanisms associated with these ranges of frequency (reciprocal of relaxation time), perhaps particularly P3, are sensitive to oxygen content in the cathode atmosphere (Table 8).

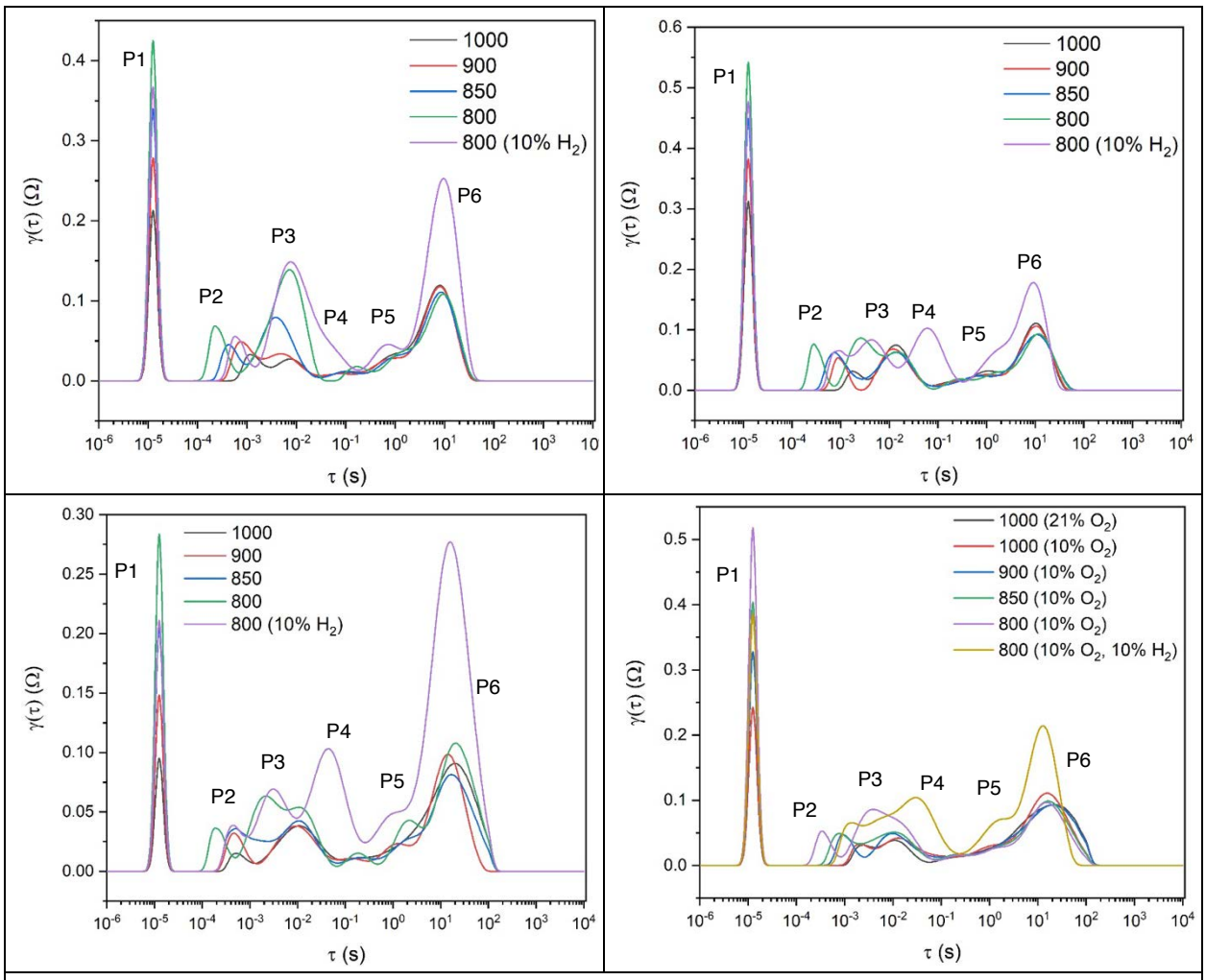

Figure 37. DRT analyses of parametric tests on four cells with LSM 80-95 cathodes, two in air (top row) and two with 10% oxygen (bottom row) as the cathode atmosphere.

Figure 38 shows how the DRT analyses of the same four cells as Figure 37 evolved over time in their respective long-term tests. Certain features apply regardless of the cathode atmosphere. As testing progresses (*t* increasing):

- P1 increases. Since this peak is associated with ionic conductivity in YSZ, this change might reflect drops in three-phase boundary (TPB) density, associated with coarsening of the cathode microstructure over time.

- The low-frequency (high-τ) peaks P4, P5, and P6 mostly show little change, even in the longer (288-h) test at 1,000 °C and high current density (0.76 A cm^{-2}) in air (upper left).
- When changes with time were evident, they were mostly in P2, P3, and P4.

The differences between air and 10% oxygen at the cathode were most significant in the test under all-aggressive conditions — 1,000 °C, 0.76 A cm^{-2}, 10% oxygen (Fig. II, bottom left). The shift of P2 to shorter relaxation times, and the growth and eventual merging of P2 and P3 was

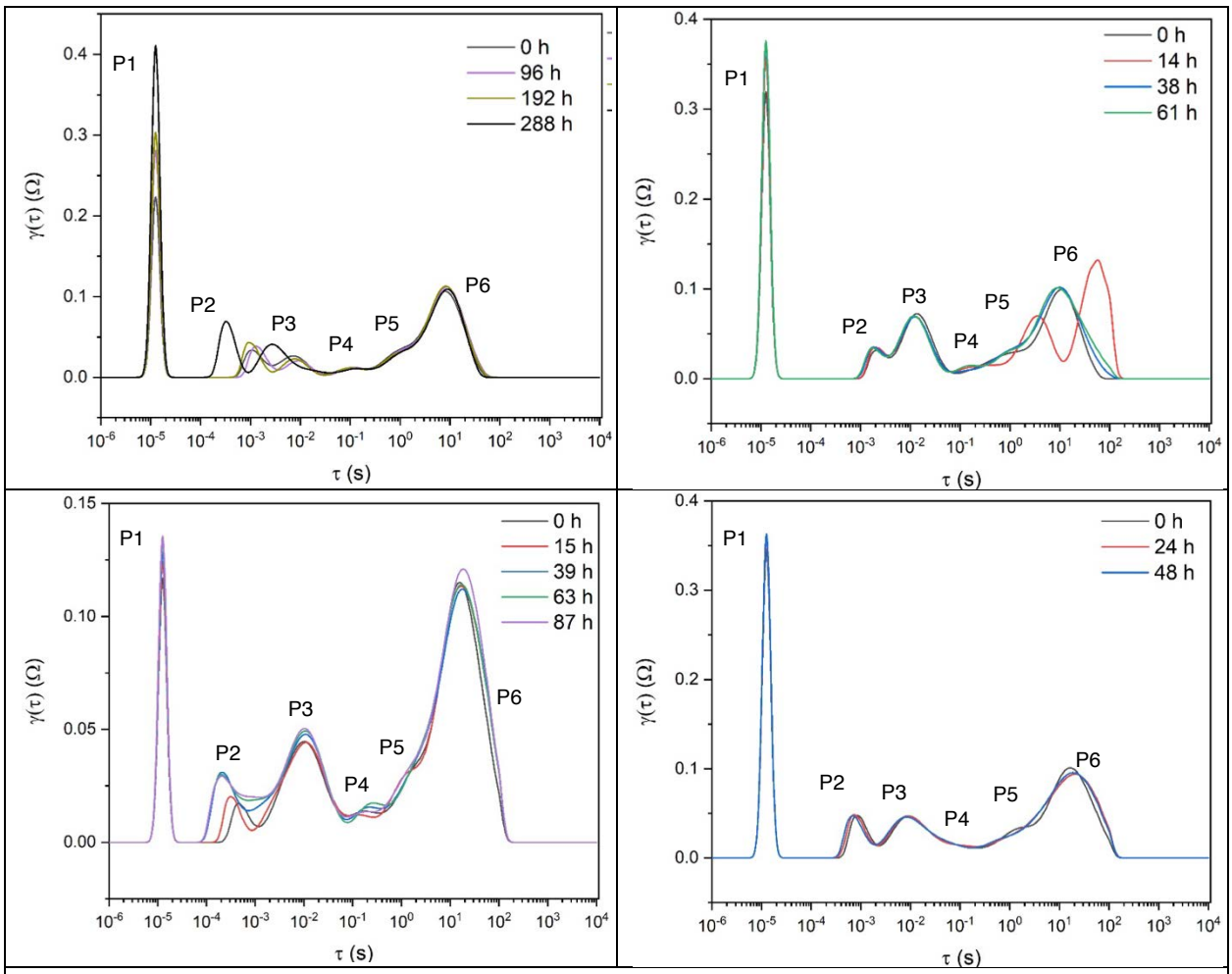

Figure 38. DRT analyses of long-term tests on four cells with LSM 80-95 cathodes, two at 1,000 °C in air, 0.76 A cm^{-2} (top row) and two with 10% oxygen (bottom row) as the cathode atmosphere. Left bottom: 1,000 °C, 0.76 A cm^{-2}; right bottom: 900 °C, 0.38 A cm^{-2}.

evident in less than 90 h under these conditions. As with the changes in these peaks with temperature (Figure 37), this indicates that the loss mechanisms in this range of frequencies become stronger with reduced oxygen in the cathode atmosphere (Table 8).

DRT analysis: Effect of temperature. It is well known that at higher temperature, both ionic transport (in YSZ) and reaction kinetics (at the electrodes) are enhanced. This results in a decrease in both series resistance and cathode resistance, and thus a decrease in overall resistance, as the results of parametric tests discussed above (Fig. 37) clearly showed.

Comparison with prior project; specimen-to-specimen variability. Figures 39 and 40 each compare the electrode ASR versus time in a successful long-term test from the prior project with a similar test from the current work. The LSM formulation was the same between the cells in each figure, but there was a difference in each case.

- In Figure 39, the cell in the earlier test had a YSZ electrolyte that was twice as thick (200 µm) as the cell in the current test (100 µm, the same as all the cells tested here and as the non-LSM-85-90 cells in the prior work). The effect of the thicker electrolyte has been

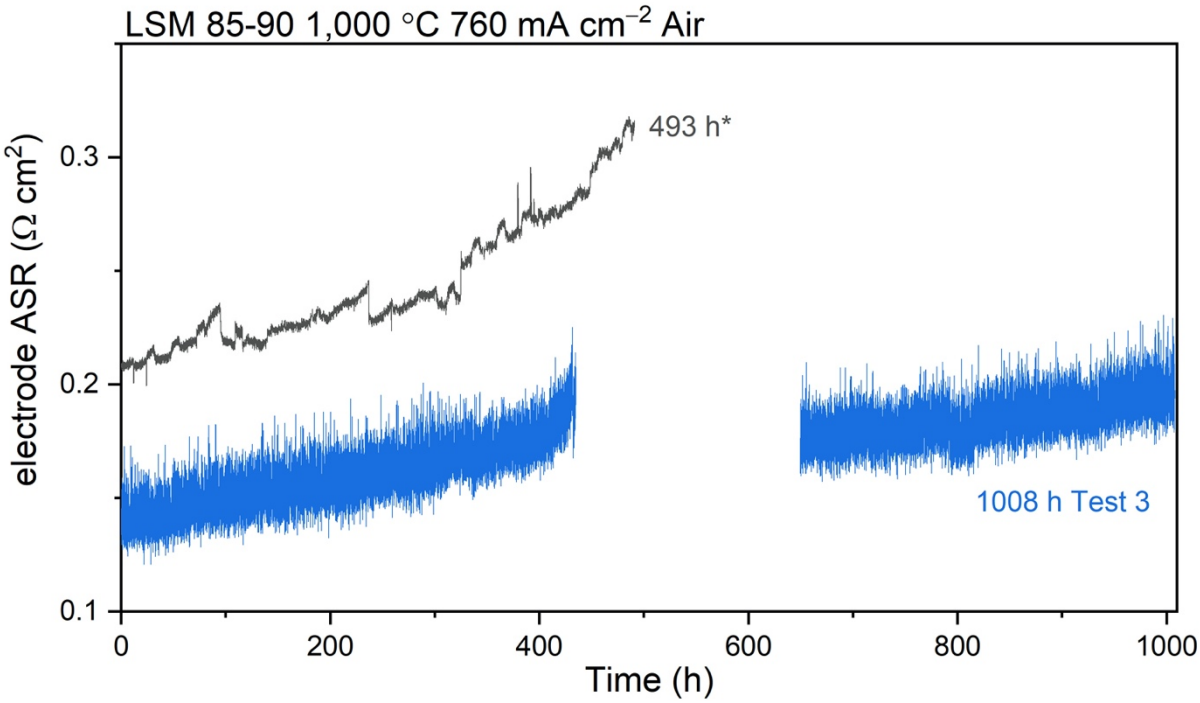

Figure 39. Long-term durability testing of cells with LSM 85-90 cathodes at 1,000 °C, 0.76 A cm^{-2} in air. Asterisk denotes a test from the prior project; the 1,008-h test (blue) is from the current work.

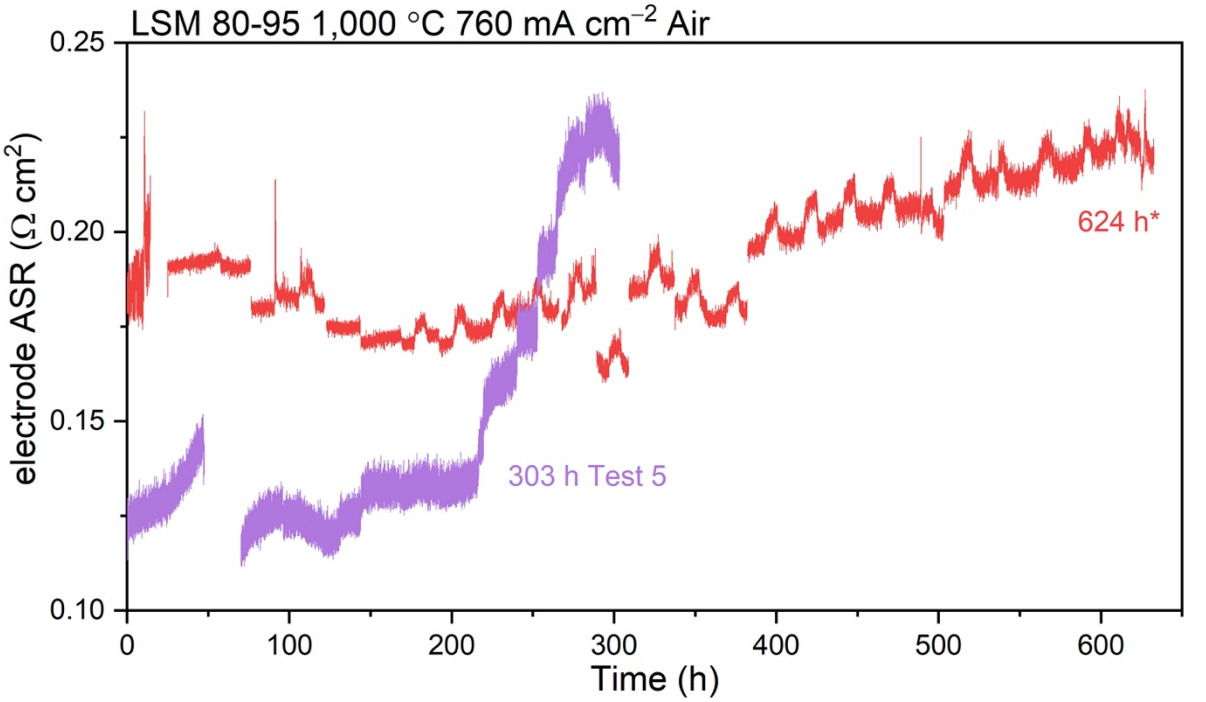

Figure 40. Long-term durability testing of cells with LSM 80-95 cathodes at 1,000 °C, 0.76 A cm^{-2} in air. Asterisk denotes a test from the prior project; the 1,008-h test (purple) is from the current work.

compensated by plotting electrode ASR only, as discussed in the Approaches section (Table 1).

- In Figure 40, the rapid rise in electrode ASR after 200 h in the test from the current work was attributed to a drop in furnace temperature because of gradual thermocouple oxidation.

Despite these differences, it is still evident that differences in performance from cell to cell with the same cathode formulation can be as large as differences in performance between cells of different cathode compositions.

Summary and conclusions

The electrochemical performance of solid oxide fuel cells, with cathodes containing three different compositions of lanthanum strontium manganite (LSM), were examined under different temperatures (1,000 °C, 900 °C), current densities (no load, 380 mA cm^{-2}, 760 mA cm^{-2}), and cathode atmospheres ($p_{O_2} = 0.10, 0.15, 0.21$) for durations ranging from a few days to 1,008 h (six weeks). The cells were electrolyte-supported, lab-scale button cells with yttria-stabilized zirconia (YSZ) electrolytes, LSM/YSZ composite cathodes, and nickel/YSZ composite anodes. The microstructures of the tested cells were examined using scanning electron microscopy and energy-dispersive x-ray spectroscopy (SEM/EDS).

Low temperature and low partial pressure of oxygen led to higher initial area specific resistance (ASR) in the cells, whether measured from the change in cell output voltage versus time (ASR_{DC}), from equivalent circuit fits to EIS data (one or two arcs) (ASR_{EIS}), or from the slope of *V-I* curves (ASR_{LSV}). The ASR, a primary measure of cell performance loss, increased with time in all cells regardless of test conditions (temperature, current density, and cathode atmosphere). A cell with an LSM 85-90 cathode, tested for 1,008 h at 1,000 °C, 760 mA cm^{-2} in air, showed a degradation rate of 22.2% ASR rise per kh, while a cell with an LSM 80-95 cathode tested at low temperature (900 °C), low current density (380 mA cm^{-2}), and low partial pressure of oxygen ($p_{O_2} = 0.10$) for 58 h showed a degradation rate of 65% per kh. Cells that exhibited high initial values of total cell ASR (above 0.4 Ω cm^2) also exhibited early cell failure (< 100 h), forcing an end to those tests.

Electrochemical impedance spectroscopy (EIS) measurements were performed every 24 h during the tests. The total cell ASR from EIS was separated (using equivalent circuit fitting of Nyquist plots) into series resistance R_s (ionic transport in YSZ) and parallel resistances R_p (electrochemical processes related to the anode and cathode). Both R_s and R_p were higher at low temperature and low p_{O_2} regardless of LSM compositions. Distribution of relaxation of times (DRT) analysis was performed to investigate the electrochemical processes and their corresponding relaxation frequencies as well as their attributions to the total ASR. Loss mechanisms with characteristic frequencies above 10,000 Hz were attributed to the electrolyte, whereas peaks at lower frequencies (< 1 Hz) were attributed to losses from transport of the cathode and anode gases. Peaks that occurred between 10,000 Hz and 1 Hz were attributed to cathodic and anodic processes, because of their increases when either the hydrogen content of the anode gas or oxygen content of the cathode gas were reduced from the standard condition (100% hydrogen or air, respectively). The areas of these peaks generally increased with time during individual tests.

Three ways of quantifying ASR were compared as metrics of degradation during extended testing: ASR_{DC}, ASR_{EIS}, and ASR_{LSV}. All three tracked with each other similarly with time, both in

short-term and in long-term trends, and responded similarly with differences in the operating conditions (temperature, current density, and cathode atmosphere). Values of ASR_{DC} were uniformly higher than those of ASR_{EIS} and ASR_{LSV}, though ASR_{DC} was only slightly higher than ASR_{EIS} for the 1,008-hour test.

The LSM compositions were:

- (La0.85Sr0.15)0.90MnO3±δ (LSM 85-90)
- (La0.80Sr0.20)0.95MnO3±δ (LSM 80-95)
- (La0.80Sr0.20)0.98MnO3±δ (LSM 80-98)

The effects of LSM composition on performance were smaller than sample-to-sample differences between cells with the same LSM composition, so no clear relationships could be discerned between cell degradation and LSM composition in this work.

Microstructural analysis showed that formation of manganese oxide (MnO_x) particles, or coarsening of existing particles, were observed after prolonged testing at high temperature and high current density in air (LSM 85-90, 1,008 h) as well as after testing under low p_{O_2} for a shorter time (LSM 80-95, 58 h, 10% O_2). As previously observed, the amount of MnO_x increased with increasing amount of Mn excess in the LSM composition (i.e., LSM 80-98 < LSM 80-95 < LSM 85-90). However, the role of MnO_x in cell degradation (if any) is still unknown. Its tendency to accumulate at the cathode/electrolyte interface during operation, which is probably associated with the lower oxygen content of the cathode stream at that location in the cell, may coincide with an observed tendency for loss of porosity at both the cathode/electrolyte interface and the cathode/cathode current collector (CCC) interface. This microstructural change was observed in the current work as well as in the preceding related project ("Long Term Degradation of LSM Based SOFC Cathodes: Use of a Proven Accelerated Test Regimen," DE-FE0023476, October 2014 – March 2019) and could be a true cause of long-term degradation of performance associated with LSM-based cathodes. The observed MnO_x particles might therefore be more of a symptom, rather than a cause, of microstructure-related performance loss.

References cited

1 San Ping Jiang, "Development of lanthanum strontium manganite perovskite cathode materials of solid oxide fuel cells: a review," *J. Mater. Sci.* **43**, 6799–6833 (2008).

2 Harumi Yokokawa, Hengyong Tu, Boris Iwanschitz, Andreas Maic, "Fundamental mechanisms limiting solid oxide fuel cell durability," *J. Power Sources* **182** pp. 400-412 (2008).

3 X.-D. Zhou, S. P. Simner, J. W. Templeton, Z. Nie, J. W. Stevenson, and B. P. Gorman, "Electrochemical Performance and Stability of the Cathode for Solid Oxide Fuel Cells. II. Role of Ni Diffusion on LSM Performance," *J. Electrochem. Soc.* **157 [**5] B643–B649 (2010).

4 S. Lee, N. Miller, H. Abernathy, K. Gerdes, A. Manivannan, "Control of Electrode Activity of SOFC Cathode Functional Layer Composed of SDC-LSCF through Infiltration," *J. Electrochem. Soc.* **158** [6] pp. B735-B742 (2011).

5 X.-D. Zhou, S. P. Simner, J. W. Templeton, Z. Nie, J. W. Stevenson, and B. P. Gorman, "Electrochemical Performance and Stability of the Cathode for Solid Oxide Fuel Cells. II. Role of Ni Diffusion on LSM Performance," *J. Electrochem. Soc.* **157 [**5] B643–B649 (2010).

6 M. Backhaus-Ricoult, "Interface chemistry in LSM–YSZ composite SOFC cathodes," *Solid State Ionics* **177** 2195–2200 (2006).

7 M. Backhaus-Ricoult, K. Adib, T. St.Clair, B. Luerssen, L. Gregoratti, A. Barinov," *In-situ* study of operating SOFC LSM/YSZ cathodes under polarization by photoelectron microscopy" *Solid State Ionics* **179** 891–895 (2008).

8 James R. Wilson, Anh T. Duong, Marcio Gameiro, H. J. Wang, Hsun-Yi Chen, Katsuyo Thornton, Daniel R. Mumm, Scott A. Barnett, "Quantitative three-dimensional microstructure of a solid oxide fuel cell cathode," *Electrochem. Comm.* **11** 1052–1056 (2009).

9 Y. L. Liu, A. Hagen, R. Barfod, M. Chen, H, F. W. Poulsen, P. V. Hendriksen, "Microstructural Studies on Degradadtion of Interface between LSM-YSZ Cathode and YSZ Electrolyte in SOFCs," *Solid State Ionics* **180** 1298–1304 (2009).

10 R. Knibbe, J. Hjelm, M. Menon, N. Pryds, M. Søgaard, H. J. Wang, K. Neufeld, "Characterizations of Cathode-Electrolyte Interfaces of CGO Barrier Layers in SOFC," *J. Am. Ceram. Soc.* **93** [9] 2877–2883 (2010).

11 James R. Wilson, J. Scott Cronin, Anh T. Duong, Sherri Rukes, Hsun-Yi Chen, Katsuyo Thornton, Daniel R. Mumm, Scott Barnett, "Effect of composition of ($La_{0.8}Sr_{0.2}MnO_3$–Y_2O_3-stabilized ZrO_2) cathodes: Correlating three-dimensional microstructure and polarization resistance" *J. Power Sources* **195** 1829–1840 (2010).

12 A. Hessler-Wyser, Z. Wuillemin, J. A. Schuler, A. Faes, J. Van herle, "TEM investigation on zirconate formation and chromium poisoning in LSM/YSZ cathode," *J. Mater. Sci.* **46** 4532–4539 (2011).

13 George J. Nelson, William M. Harris, Jeffrey J. Lombardo, John R. Izzo Jr., Wilson K.S. Chiua, Pietro Tanasini, Marco Cantoni, Jan Van herle, Christos Comninellis, Joy C. Andrews, Yijin Liu, Piero Pianetta, Yong S. Chu, "Comparison of SOFC cathode microstructure quantified using X-ray nanotomography and focused ion beam–scanning electron microscopy," *Electrochem. Commun.* **13** [6] 586–589 (2011).

14 J. S. Cronin, Y. C. K. Chen-Wiegart, J. Wang, and S. A. Barnett, "Three-dimensional reconstruction and analysis of an entire solid oxide fuel cell by full-field transmission X-ray microscopy," *J. Power Sources* **233 174-179** (2013).

15 M. Naslund and H. Iskov. *Accelerated Lifetime Testing and Standardization of SOFC Systems*. Rep. no. 734-90. Danish Gas Technology Centre, 2012.

16 A. Weber, J. Szász, S. Dierickx, C. Endler-Schuck, and E. Ivers-Tiffee. "Accelerated lifetime tests for SOFCs," *ECS Transactions* **68** [1] pp. 1953–960 (2015).

17 Zhien Liu and Ted Ohrn, "Progress on Performance, Durability, and Reliability of LGFCS SOFC Technology," presented at the 14th Annual Solid State Energy Conversion Alliance (SECA) Workshop, Pittsburgh, Pennsylvania, 23 July 2013. (https://netl.doe.gov/sites/default/files/event-proceedings/2013/seca/Ohrn-Liu-2013-SECA-workshop_Final.pdf

18 Hsiang-Jen Wang, Naima Hilli, Mark R. De Guire, Richard Goettler, Zhien Liu, Zhengliang Xing, Theodore R. Ohrn, and Arthur H. Heuer, "Microstructural Evolution in LSM-YSZ Cathodes over Two Years of SOFC Operation," presented at the 14th Annual Solid State Energy Conversion Alliance (SECA) Workshop, Pittsburgh, Pennsylvania, 23-24 July 2013. (http://www.netl.doe.gov/File%20Library/events/2013/seca/Wang.pdf).

19 Celeste E. Cooper, "Degradation in Performance of Lanthanum Strontium Manganite Based Solid Oxide Fuel Cell Cathodes Under Accelerated Testing," M.S. thesis, Case Western Reserve University, May 2017.

20 Chenxin Deng, "Operating Stresses and their Effects on Degradation of LSM-Based SOFC Cathodes," M.S. thesis, Department of Materials Science and Engineering, Case Western Reserve University, August 2021.

21 B. A. Boukamp, "A Linear Kronig-Kramers Transform Test for Immittance Data Validation," *J. Electrochem. Soc.*, **142** [6] p. 1885 (1995). doi: 10.1149/1.2044210.

22 A. Weiß, S. Schindler, S. Galbiati, M. A. Danzer, and R. Zeis, "Distribution of Relaxation Times Analysis of High-Temperature PEM Fuel Cell Impedance Spectra," *Electrochimica Acta*, **230**, pp. 391–398 (Mar. 2017). doi: 10.1016/j.electacta.2017.02.011.

23 S. Dierickx, A. Weber, and E. Ivers-Tiffée, "How the distribution of relaxation times enhances complex equivalent circuit models for fuel cells," *Electrochimica Acta*, **355**, p. 136764, (Sep. 2020). doi: 10.1016/j.electacta.2020.136764.

24 T. Wan, M. Saccoccio, C. Chen, and F. Ciucci, "Influence of the Discretization Methods on the Distribution of Relaxation Times Deconvolution: Implementing Radial Basis Functions with DRTtools," *Electrochimica Acta*, **184** (Oct. 2015). doi: 10.1016/j.electacta.2015.09.097.

25 Madeleine McAllister, "Electrochemical Impedance Spectroscopy and Distribution of Relaxation Times Analysis of Solid Oxide Fuel Cells," CWRU, Senior project final report (unpublished work), Dec. 2019.

26 R. M. Ormerod, "Solid oxide fuel cells," *Chem. Soc. Rev.*, **32** [1] pp. 17–28 (2003). doi: 10.1039/B105764M.

27 V. Sonn, A. Leonide, and E. Ivers-Tiffée, "Combined Deconvolution and CNLS Fitting Approach Applied on the Impedance Response of Technical Ni/8YSZ Cermet Electrodes," *J. Electrochem. Soc.* **155** [7] p. B675 (2008). doi: 10.1149/1.2908860.

28 T. Ishihara, "Development of New Fast Oxide Ion Conductor and Application for Intermediate Temperature Solid Oxide Fuel Cells," *BCSJ* **79** [8] pp. 1155–1166 (Aug. 2006). doi: 10.1246/bcsj.79.1155.

29 Leszek Wojnar, Krzysztof J. Kurzydłowski, Janusz Szala, "Quantitative Image Analysis," *Metallography and Microstructures, Vol. 9, ASM Handbook*, ASM International, pp. 403–427 (2004).

30 Mark De Guire, Naima Hilli, Hsiang-Jen Wang, Celeste Cooper, Ryan Zienert, and Arthur H. Heuer, "Long-Term Degradation of LSM-Based SOFC Cathodes: Use of a Proven Accelerated Test Regimen," presented at the 16th Annual Solid Oxide Fuel Cell Workshop, Pittsburgh, PA, Jul. 14, 2015. Available online: https://netl.doe.gov/sites/default/files/event-proceedings/2015/2015sofc/De-Guire.pdf

31 Chenxin Deng, Andrew Cai, Naima Hilli, Madeleine McAllister, Mark De Guire, and Arthur Heuer, "Effects of Manganese Excess on the Microstructure and Performance of LSM-Based SOFC Cathodes Operated under Aggressive Conditions," presented at Materials Science & Technology 2018, Columbus, Ohio, Oct. 17, 2018.

32 A. Hagen, Y. L. Liu, R. Barfod, and P. V. Hendriksen, "Assessment of the Cathode Contribution to the Degradation of Anode-Supported Solid Oxide Fuel Cells," *J. Electrochem. Soc.*, vol. 155, no. 10, p. B1047, 2008, doi: 10.1149/1.2960938.

33 H. Sumi, H. Shimada, Y. Yamaguchi, T. Yamaguchi, and Y. Fujishiro, "Degradation evaluation by distribution of relaxation times analysis for microtubular solid oxide fuel cells," *Electrochimica Acta*, vol. 339, p. 135913, Apr. 2020, doi: 10.1016/j.electacta.2020.135913.

34 R. Barfod, A. Hagen, S. Ramousse, P. V. Hendriksen, and M. Mogensen, "Break Down of Losses in Thin Electrolyte SOFCs," *Fuel Cells*, vol. 6, no. 2, pp. 141–145, 2006, doi: 10.1002/fuce.200500113.

35 R. Barfod, M. Mogensen, T. Klemensø, A. Hagen, Y.-L. Liu, and P. V. Hendriksen, "Detailed Characterization of Anode-Supported SOFCs by Impedance Spectroscopy," *J. Electrochem. Soc.*, vol. 154, no. 4, p. B371, Feb. 2007, doi: 10.1149/1.2433311.

36 V. Sonn, A. Leonide, and E. Ivers-Tiffée, "Combined Deconvolution and CNLS Fitting Approach Applied on the Impedance Response of Technical Ni/8YSZ Cermet Electrodes," *J. Electrochem. Soc.*, vol. 155, no. 7, p. B675, May 2008, doi: 10.1149/1.2908860.

37 M. Riegraf, R. Costa, G. Schiller, K. A. Friedrich, S. Dierickx, and A. Weber, "Electrochemical Impedance Analysis of Symmetrical Ni/Gadolinium-Doped Ceria (CGO10) Electrodes in Electrolyte-Supported Solid Oxide Cells," *J. Electrochem. Soc.*, vol. 166, no. 13, Art. no. 13, 2019, doi: 10.1149/2.0051913jes.

38 M. P. Carpanese *et al.*, "Understanding the electrochemical behaviour of LSM-based SOFC cathodes. Part I — Experimental and electrochemical," *Solid State Ionics*, vol. 301, pp. 106–115, Mar. 2017, doi: 10.1016/j.ssi.2017.01.007.